Analysis, Design and Construction of an LLC Resonant Converter

by

Shi Pu

A thesis submitted to the Graduate Faculty of
Auburn University
in partial fulfillment of the
requirements for the Degree of
Master of Science

Auburn, Alabama
May 7, 2016

Keywords: LLC resonant converters, Soft switching
Electromagnetic design, Small-signal modeling

Approved by

Robert Mark Nelms, Chair, Professor, Electrical Engineering
John York Hung, Professor, Electrical Engineering
Michael Edward Baginski, Associate Professor, Electrical Engineering

Abstract

The trend in DC/DC converters development is toward higher frequency, power density and efficiency. The traditional hard-switched converter is limited in switching frequency and power density. The phase-shift full-bridge PWM Zero-voltage-switching (ZVS) converter has been used widely because of its ZVS working condition. But it has a problem due to the reverse recovery of the diodes, which reduces its efficiency. Nowadays, the LLC resonant converter is a popular research field to consider for increasing converter efficiency.

In this thesis, the conditions to achieve the ZVS mode of the LLC resonant converter are studied using the method of fundamental element simplification. Six different conducting stages have been introduced individually and analyzed. Also, the operating region of the LLC resonant converter has been studied, along with the relationship between the input and output voltage as affected by the load and the switching frequency.

After analyzing the DC characteristics of the LLC resonant converter, its small signal model is presented and is developed using the method of extended describing functions. Using this model, a voltage control was designed and implemented using an MC34066 analog control chip. A prototype LLC resonant converter was constructed and tested in the laboratory.

Acknowledgments

I would like to thank my advisor, Dr. R. Mark Nelms for his patient guidance. The most precious thing I learned from him is the attitude toward research and life, having the courage to explore. He let me realize that failure is not despair, but hope.

I also appreciate my committee members: Dr. John Y. Hung, Dr. Michael E. Baginski for their help and valuable suggestions.

I am very grateful to my parents, Anshan Pu and Jianhong Li, who have been encouraging and supporting me to pursue my goal.

Table of Contents

List of Figures

List of Tables

CHAPTER 1. Introduction

The main goal of power electronics is to apply power electronic devices and control technologies to manage and convert electric energy. Being a combination of electronic technology, control technology and power technology, power electronics has great technical and economic significance.

1-1. Basic principles of switch-mode power supplies (SMPS)

Power converters can be divided into four types:

- Rectifiers (AC/DC): A rectifier converts an AC voltage to a DC voltage. Rectifying means the power flows from the AC side to the DC side.
- Inverters (DC/AC): An inverter converts a DC voltage to an AC voltage. For example, an uninterruptible power supply can provide an AC voltage to a load from the DC stored in batteries.
- AC/AC converter: it can change both the frequency and magnitude of its AC input voltage.
- DC/DC converter: In a dc-dc converter, the dc input voltage is converted into to a dc output voltage at another level [1].

1-2. Resonant mode conversions

Interest in switched-mode power supplies (SMPS) has been skyrocketing during the past few decades. Resonant converters have been utilized widely in power electronics industry till now. Over the years we have seen power conditioning move from simple but extravagant linear

regulators, through early low frequency pulse-width modulated systems, to high frequency square wave converters which pack the same power handling capabilities of earlier designs into a fraction of their size and weight. Today, a new approach is upon us the resonant mode converter. While offering new benefits in performance, size, and cost, this new technology brings with it an added dimension of complexity [2]. There are several commonly seen and used resonant converters, but in this thesis we focus on the LLC resonant converter.

- Series resonant converter: A series resonant converter has a resonant tank formed by a resonant capacitor and a resonant inductor. This circuit and its derivatives are among the most simple and least costly to produce converter circuits, but it has some disadvantages as it cannot operate when the circuit is unloaded.
- Parallel resonant converter: The characteristics of the parallel resonant converter are quite different from those of the series resonant converter, and from those of conventional PWM converters [2]. It has a resonant tank formed by a resonant capacitor and a resonant inductor that are parallel connected. The voltage gain during its operating process can be either larger or smaller than 1, which makes it popular for applications that requires variable output voltage. However it has a relatively much higher power loss than other resonant converters.
- LLC resonant converter: The traditional topologies of resonant conversion can optimize performance at one operating point, but not with wide range of input voltages and load power variations. LLC resonant converter can operate over a larger range of input voltage and switching frequency. Also, in a high voltage mode, the LLC resonant converter has a

higher efficiency than SRCs and PRCs.

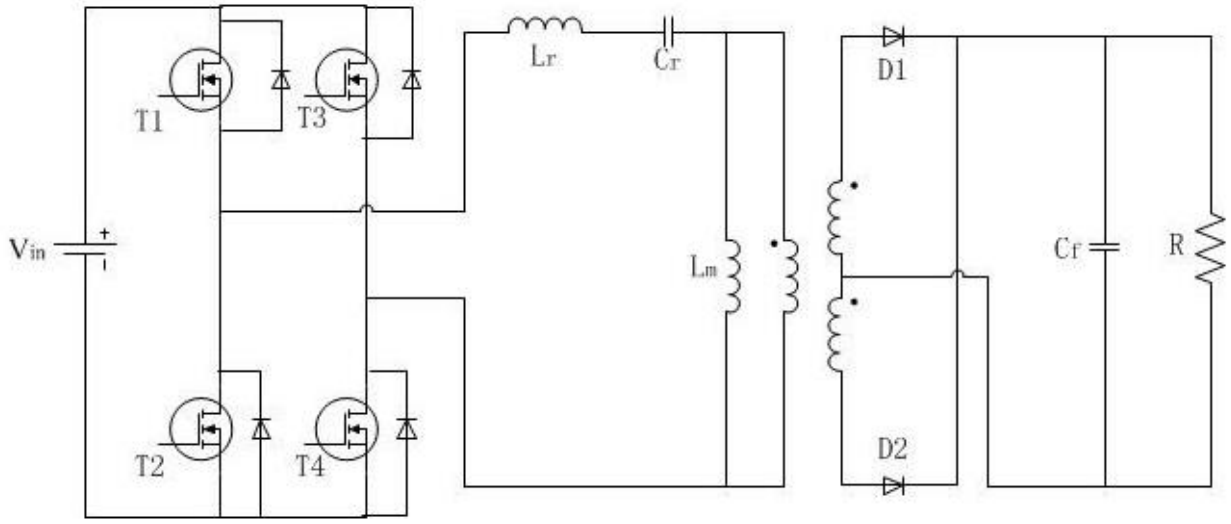

Fig 1.1 Circuit diagram of an LLC resonant converter

1-3. Organization of this thesis

This thesis is organized as follows:

The fundamental characteristics of LLC resonant converters are illustrated in Chapter 2. An equivalent circuit is presented, and its mathematical model is constructed. Six different operating stages are illustrated and certain operating regions will be discussed. Also, properties of MOSFETs and IGBTs are discussed. This is key in the selction of the semiconductor switches for the LLC resonant converter.

The small signal modeling of the LLC resonant converter is presented in Chapter 3. Several methods are briefly introduced, and the method of extended describing function is described in detail. Applying the extended describing function method to LLC resonant converter yields a small signal model. A control strategy is also discussed.

Chapter 4 is mainly focused on the design and construction of an open-loop converter. Litz

wire was utilized in the construction of the transformer in the LLC resonant converter. Circuit parameters were chosen based on the characteristics discussed in chapter 2. Also, an analog-control chip is selected to regulate the output voltage of the LLC resonant converter.

Test results for the prototype converter are presented in Chapter 5.

Conclusions and suggestions for future work are given in Chapter 6.

CHAPTER 2. Basic principle of LLC resonant converters

In recent years, LLC resonant converters have been widely used in power grids, renewable energy systems and common appliances. As mentioned in Chapter 1, SRCs and PRCs have disadvantages like power loss in resonant tanks. In 1990s, researchers have proposed multi-resonant converters like LCC and LLC resonant converters. An LLC resonant converter can operate stably when the input voltage and load vary over a wide range. Also, its switches operates in ZVS mode, which can reduce the power loss during conduction. Even compared to phase-shifted full-bridge converters, which are commonly seen in power systems, the LLC converter has higher efficiency due to its being free from the reverse recovery problem of diodes [3]. As a result, LLC resonant converters are commonly used in distributed power systems to maintain the stability of the power grid.

2-1. Performance comparison between MOSFET and IGBT

MOSFETs and IGBTs are widely used in high frequency power converters. As majority carrier devices, they are free from charge storage effect and have a high switching speed. In addition, they have high input impedance and low driving power at the same time. MOSFETs are more appropriate for high-frequency switch-mode power supplies, because they have a relatively higher operating speed than IGBTs.

Figure 2.1(a) shows the internal structure of both a MOSFET and an IGBT. Figure 2.1 (b) shows the equivalent circuits of both. Compared to a MOSFET, the IGBT has an extra layer P+, leading directly into the collector [4].

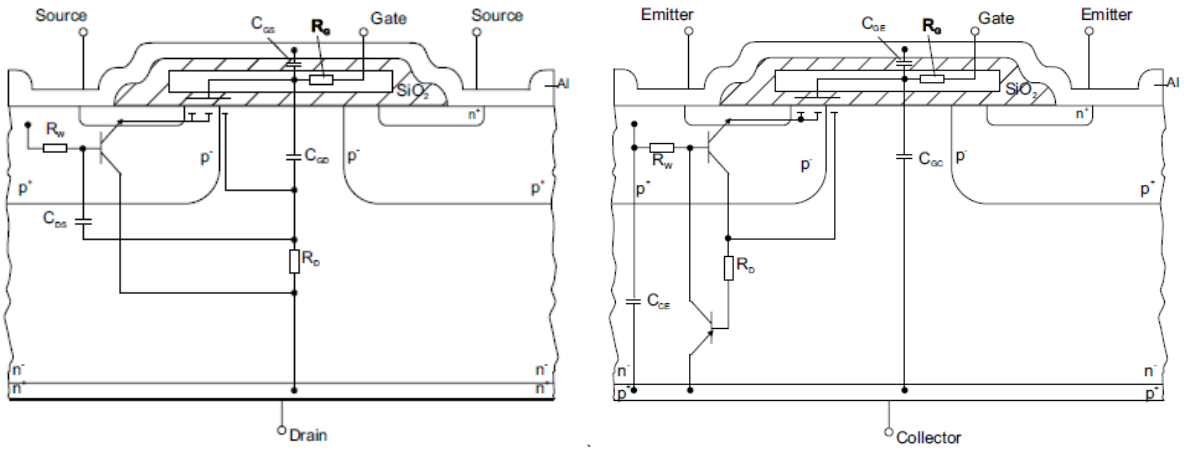

Fig 2.1(a) Internal structures for a MOSFET and an IGBT[5]

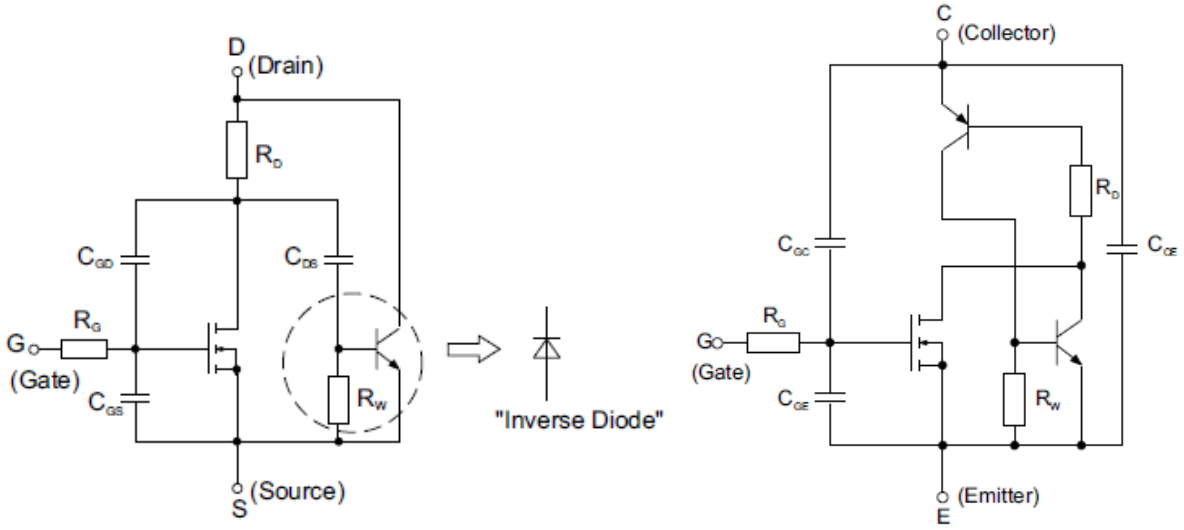

Fig 2.1(b) Equivalent circuits for a MOSFET and an IGBT[5]

The physical causes and designations of the parasitic capacitances and resistances shown in Figure 2.1 are evident in Table 2.1(a) and Table 2.1(b)

Symbol	Designation	Physical Description
C_{GS}	Gate-source capacitance	Overlapping gate and source metallisation; dependent on gate-source voltage; independent of drain-source voltage
C_{DS}	Drain-source capacitance	Junction capacitance between n^- drift area and p-well; dependent on cell surface, breakdown voltage and drain-source voltage
C_{GD}	Gate-drain capacitance	Miller capacitance; generated by overlapping of gate and n^- drift area
R_G	Internal gate resistance	Polysilicon gate resistance; additional series resistors are often needed in modules with several transistor chips to minimise oscillations between chips
R_D	Drain resistance	Resistance of n^- region; often the main part of MOSFET on-state resistance
R_W	Lateral resistance of the p-well	Base-emitter resistance of the parasitic bipolar NPN transistor

Table 2.1(a) Physical causes and designations of a MOSFET parasitic elements[5]

Symbol	Designation	Physical Description
C_{GE}	Gate-emitter capacitance	Overlapping gate and source metallisation; dependent on gate-emitter voltage; independent of collector-emitter voltage
C_{CE}	Collector-emitter capacitance	Junction capacitance between n^- drift area and p-well; dependent on cell surface, breakdown voltage and drain-source voltage
C_{GC}	Gate-collector-capacitance	Miller capacitance; generated by overlapping of gate and n^--drift area
R_G	Internal gate resistance	Polysilicon gate resistance; additional series resistors are often needed in modules with several transistor chips to minimise oscillations between chips
R_D	Drift resistance	Resistance of the n^- region (base resistance of the PNP transistor)
R_W	Lateral resistance of the p-well	Base-emitter resistance of the parasitic bipolar NPN transistor

Table 2.1(b) Physical causes and designations of an IGBT parasitic elements[5]

During the switching process, the output capacitor is mainly formed of the Miller capacitance Cgd whose intensity is determined by the reverse transfer capacitance Crss which is equal to Cgd [4]. In a certain operating region, higher Crss will result in more intense Miller Effect and higher output capacitance. In a MOSFET, Crss is only determined by Cgd, which depends on the structure. Nevertheless, due to the additional P^+ layer of IGBT, there is a C_{PN}

formed between the P^+ layer and N^- layer (formed by both barrier capacitance and diffusion capacitance). The equivalent capacitance of the IGBT is the series capacitance of Cgc and C_{PN}, making it smaller than a MOSFET.

For an IGBT, electrons flow through the drift region and enter the P^+ region, leaving holes (positive charge carriers) flowing into the N^- region. These injected holes flow through the MOS drain and N well into the emitter. Unlike a MOSFET, after the emitter current has stopped, many p-charge carriers generated by injection from the IGBT collector area are still present in the n-drift area. They must recombine or be reduced to zero by backward injection, which causes a more or less strong collector tail current [5]. In conclusion, a MOSFET has a bigger output capacitance, while the IGBT has a problem of tail current.

From the analysis above, it can be seen that IGBT has a relatively smaller output capacitance, and it stores less energy during the off-stage, which leads to less turn-on power loss. As a unipolar device, a MOSFET can take away charge on the input capacitor (Cgs+Cgd) instantly, accelerating the turn-off process. The IGBT will suffer the tail current problem causing a turn-off power loss.

Hence, circuits using MOSFETs as switching components should operate in the ZVS mode. In that case, before turn on, the voltage between drain and source can be zero for a low turn-on loss. Circuits using IGBTs should operate in the ZCS mode, having a zero current before turn-off, lowering the turn-off loss by the tail current.

2-2. Operating principle of the LLC resonant converter

The main circuit of the LLC series resonant converter is shown in Fig 2.2. MOSFETs are used in this full-bridge circuit.

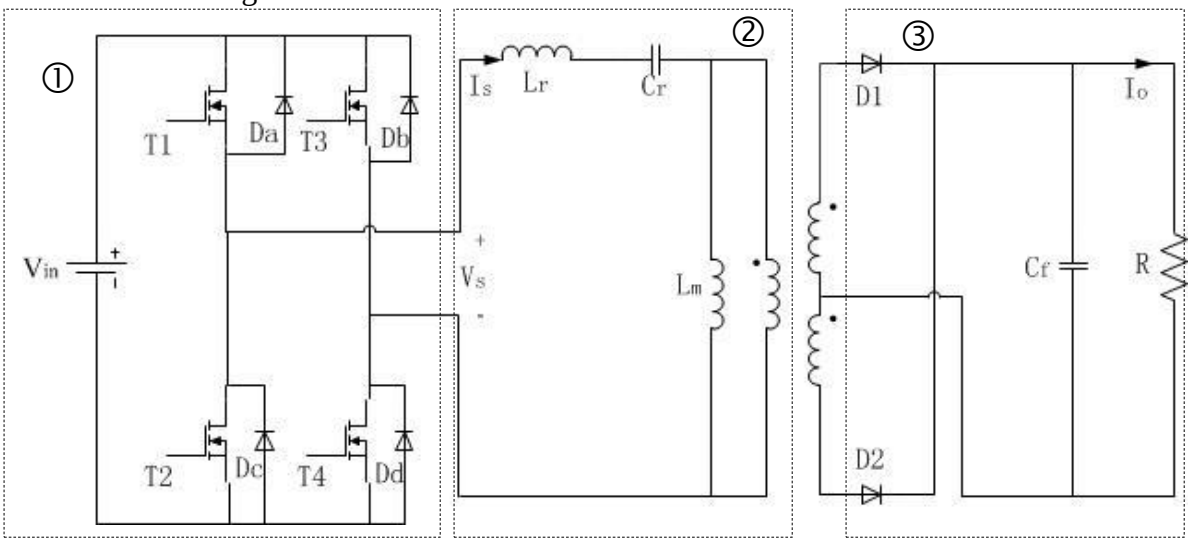

Fig 2.2 Main circuit of LLC series resonant converter

T1 and T4 share the same driving signal, and T2 and T3 share the same one. A small period of dead time between the drive signals is necessary to prevent a short circuit. L_r, C_r and L_m form the resonant tank. The secondary side is a center-tapped rectifier followed by a capacitive filter [7]. Diodes D1 and D2 form a full-wave rectifier circuit. C_f is part of the output filter. Under normal circumstances, the value of L_m is relatively high so as to play a role in filtering, replacing filter inductances on the secondary side.

If we focus on the fundamental harmonic, it will be much simpler and convenient to analyze the converter. By calculating the ratio and relationship between the first harmonic term and higher order terms, we can get the condition of ignoring higher order terms and simplify the analysis process. Thus, making assumptions that all the switches and diodes are conducting

properly and convert the load to the primary side, we get the equivalent circuit with only resonant components and load. Fig 2.3 shows equivalent circuits for the LLC resonant converter. Le and Re represent the equivalent resonant inductance and resistance of the model. The LLC resonant converter operates with a switching period of Ts, switching angular frequency of ω_s, and a resonant angular frequency of ω_r. When the switches are operated properly, we can simplify the converter circuit in Fig 2.2 to the equivalent circuit shown in Fig 2.3(a). The equivalent circuit in Fig 2.3(a) can be redrawn as Fig 2.3(b)

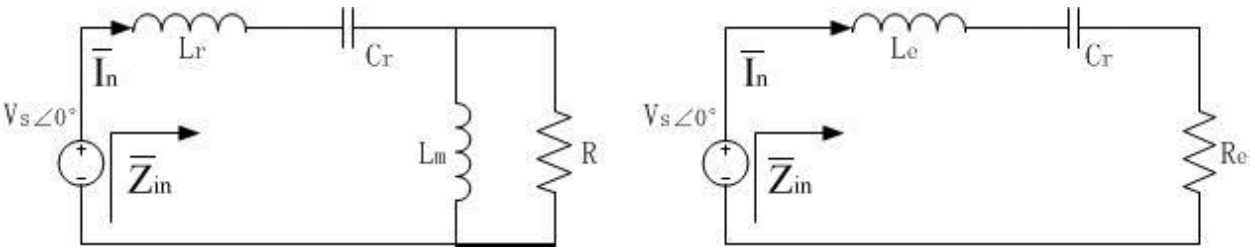

(a) (b)

Fig 2.3 Equivalent circuit model of LLC resonant converter

Combining impedance $\omega_s L_m$ and R, yields:

$$L_e = L_r + \frac{R^2 \omega_s L_m}{R^2 + \omega_s^2 L_m^2}; R_e = \frac{R \omega_s^2 L_m^2}{R^2 + \omega_s^2 L_m^2} \tag{2-1}$$

The Fourier expansion for the input voltage can be expressed as (2-3):

$$v_s(t) = \frac{4}{\pi} V_{in} \sum_{n=1}^{\infty} \frac{1}{n} \sin(n\omega_s t) \tag{2-2}$$

Also, we can determine the impedance of the equivalent circuit in Fig 2.3(b):

$$\bar{Z}_{in}(jn\omega_s) = R_e + j(n\omega_s L_e - \frac{1}{n\omega_s C_r}) \tag{2-3}$$

Since the quality factor $Q=\frac{\omega_r L_e}{R_e}$, and $\omega_r=\frac{1}{\sqrt{L_e C_r}}$, we can get the current value at different harmonics and determine the relationship between different harmonics ($\bar{I}_n$ is the nth harmonic of the current, and $\bar{I}_1$ is the fundamental component):

$$\because \left|\bar{I}_n\right|=\frac{\left|\bar{V}_{sn}\right|}{\left|\bar{Z}_{in}\right|}$$

$$\therefore \frac{\left|\bar{I}_n\right|}{\left|\bar{I}_1\right|}=\frac{\sqrt{1+\frac{Q^2\omega_s^2}{\omega_r^2}(1-\frac{\omega_r^2}{\omega_s^2})^2}}{n\sqrt{1+\frac{n^2Q^2\omega_s^2}{\omega_r^2}(1-\frac{\omega_r^2}{n^2\omega^2})^2}} \tag{2-4}$$

It can be seen from (2-5) that when Q is relatively big, ω_s approximately equals ω_r, and the current is dominated by the first harmonic. Thus, when analyzing the large-signal model, we can focus on the fundamental harmonic [1].

2-2-1 Inverter

The inverter is in block ① in Fig 2.2. We can replace the output V_s as a controlled voltage source whose value is determined by V_{in}. The equivalent circuit of the inverter is shown in Fig 2.4.

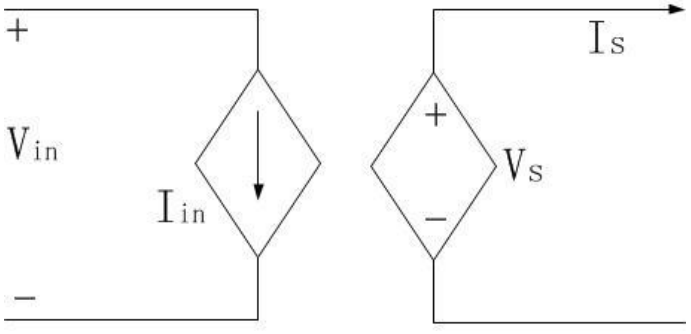

Fig 2.4 The equivalent circuit of the inverter

Being inductive, the resonant tank has an inductor current whose phase lag is φ compared to the input voltage. The fundamental harmonic of the resonant current is:

$$i_{s1}(t) = I_{s1} \sin(\omega_s t - \varphi) \tag{2-5}$$

Thus, the average current, the controlled current source in equivalent circuit of Fig 2.4 is:

$$I_{in} = \frac{2}{T_s}\int_0^{T_s/2} I_{s1} \sin(\omega_s t - \varphi)dt = \frac{2I_{s1}}{\pi}\cos\varphi \tag{2-6}$$

Since $v_{s1}(t) = \frac{4V_{in}}{\pi}\sin\omega_s t$ (2-7)

It can be included that: $P_{in} = P_{out} = \frac{2V_{in}I_{s1}}{\pi}\cos\varphi$ (2-8)

2-2-2 LLC resonant tank

The resonant tank is block ② in Fig 2.2 with the load converted to the primary side. Note that the resonant tank is connected between the input voltage and the output voltage. Thus, we can replace the resonant tank by a transfer block H(s). An equivalent diagram for the resonant tank is shown in Fig 2.5. The crucial problem part is the derivation of the transfer function H(s), which is given in (2-9).

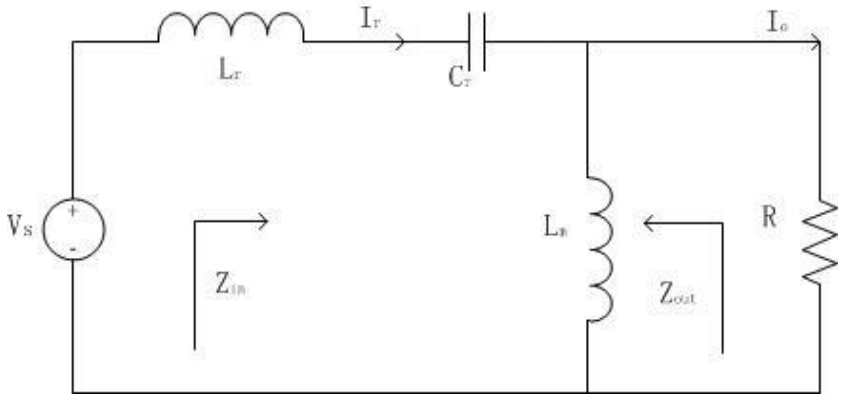

(a)

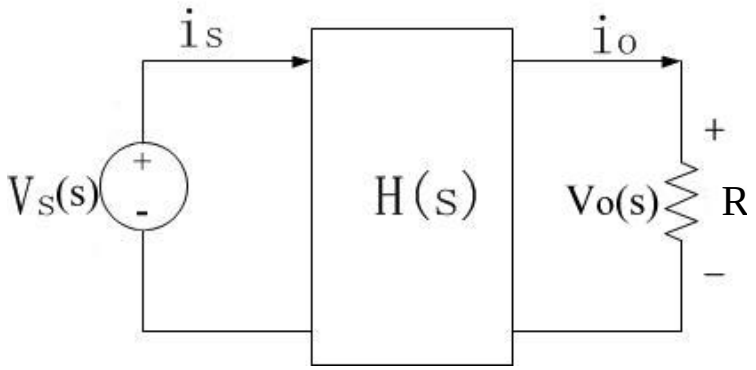

(b)

Fig 2.5 Equivalent circuits for the resonant tank

$$H(s)=\frac{V_o(s)}{V_s(s)}=\frac{\dfrac{sRL_m}{R+sL_m}}{sL_r+\dfrac{1}{sC_r}+\dfrac{sRL_m}{R+sL_m}}=\frac{s^2RC_rL_m}{s^3C_rL_rL_m+s^2C_rR(L_r+L_m)+sL_m+R} \qquad (2\text{-}9)$$

2-2-1 Rectifier

The rectifier is block ③ in Fig 2.2. Assume that the filter capacitor is large enough that it can absorb all the AC part of the output current. Also, assume that the transformer is ideal with a voltage ratio of N:1:1. The signal on the primary side is a sinusoidal, and the currents of D1 and D2 flow alternately. Because the load is modeled as a pure resistance, the phase difference between v_{p1} and i_p is 0 where v_p is the voltage across the primary side of the transformer and i_p is the current flow in the primary side of the transformer.

$$i_p(t)\approx I_{p1}\sin(\omega_s t-\psi) \qquad (2\text{-}10)$$

When $i_p>0$, D1 is on and Vp = NVo. When $i_p<0$, D2 is on and $V_p = -NV_o$. Thus, we can get the Fourier series for the primary side voltage:

$$v_p(t) \approx \frac{4NV_o}{\pi} \sum_{n=1,3,5....}^{\infty} \frac{1}{n} \sin n(\omega_s t - \phi_n) \tag{2-11}$$

Its fundamental component is $v_{p1}(t) = \frac{4NV_o}{\pi} \sin(\omega_s t - \psi)$ (2-12)

Since $R = \frac{v_{p1}(t)}{i_p(t)} = \frac{\frac{4NV_o}{\pi} \sin(\omega_s t - \psi)}{I_{p1} \sin(\omega_s t - \psi)} = \frac{4NV_o}{\pi I_{p1}}$ (2-13)

Also, the average output current is $I_o = \frac{2}{T_s} \int_0^{T_s/2} \left| NI_{p1} \sin(\omega_s t - \psi) \right| dt = \frac{2NI_{p1}}{\pi}$ (2-14)

We know that $R_L = \frac{V_o}{I_o} = \frac{\pi V_o}{2NI_{p1}}$ (2-15)

Therefore, $R = \frac{8N^2}{\pi^2} R_L$ (2-16)

As a result, $P_{in} = P_{out} = \frac{4N^2 I_{p1}{}^2}{\pi^2} R_L$, which assumes an efficiency of 100%.

Now that we have analyzed each part of the circuit in Fig 2.2, we can cascade them together to form an equivalent circuit for an LLC resonant converter based on the fundamental approximation.

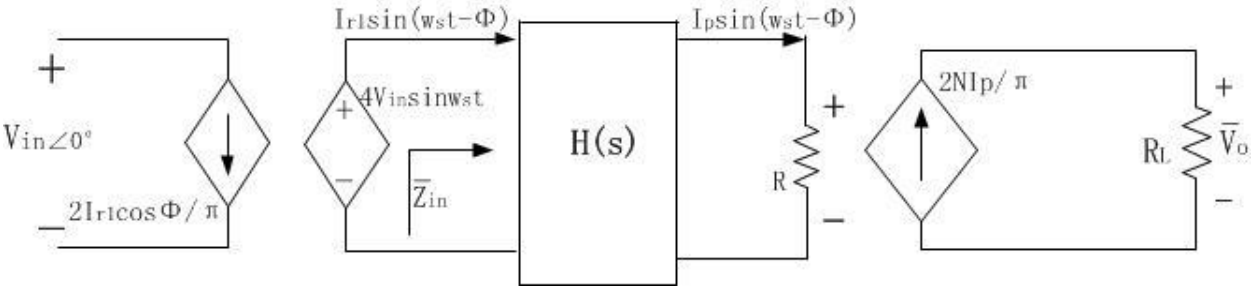

Fig 2.6 Equivalent circuit for an LLC resonant converter

From the equivalent circuit we know that the step-up ratio M is:

$$M = \frac{V_o}{V_{in}} \approx R_L \frac{2N}{\pi} \frac{\pi^2}{8N^2 R_L} \left| H(j\omega_s) \right| \frac{4}{\pi} = \frac{\left| H(j\omega_s) \right|}{N} \qquad (2\text{-}17)$$

Using MATLAB, we can plot the DC voltage characteristic of the LLC resonant converter as shown in Fig 2.7.

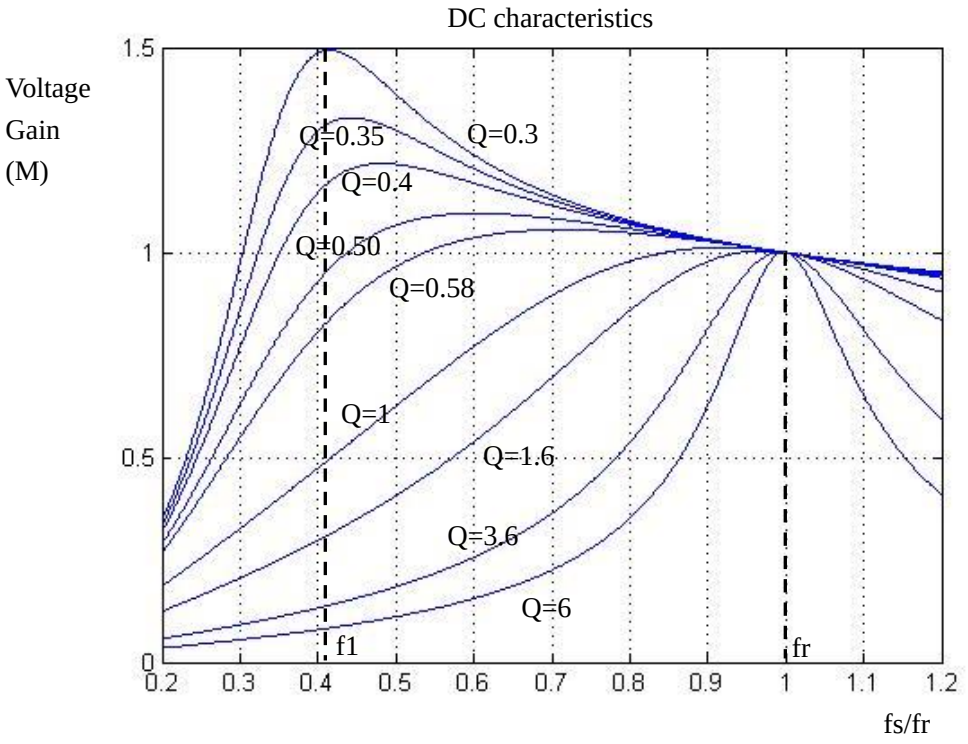

Fig 2.7 DC characteristics of the LLC resonant converters

From Fig 2.7, it can be seen that M changes with frequency. Also, there are two different resonant frequencies denoted as fr and f1. When the load becomes larger (Q becomes larger), the frequency where the peak value occurs increases.

2-3. Operating regions for the LLC resonant converter

When the MOSFETs in Fig 2.2 are driven by complementary symmetric signals and the shunt capacitance and the resonant capacitance are quite different, the conditions for ZVS and

ZCS are mainly determined by the input impedance of the resonant tank. When $\overline{Z}_{in}$ is inductive, the input current i_r lags behind the input voltage v_s by ϕ degrees. Thus, before the switches are turned on, the parasitic diodes are already conducting. As a result, the voltage across the switches is fixed to zero, realizing ZVS operation. However, when the driving signals are removed, current is still flowing in the switches, which means the turn-off stage is a hard shutdown. In contrast, when $\overline{Z}_{in}$ is capacitive, the input current i_r leads the input voltage v_s by ϕ degree. Thus, before the switches are turned on, the shunt diode of the other switch from the same bridge is conducting. As a result, the voltage across the switches is fixed to V_{in}, which means it's a hard turn on. However, when the driving signal is removed, the resonant current flows through the parasitic diode resulting in ZCS mode.

Once the load and circuit parameters have been determined, the impedance $\overline{Z}_{in}$ is determined and can't be changed. Thus, an LLC resonant converter doesn't have the ability to switch its operating mode between ZVS and ZCS. Since the imaginary part of the input impedance $\overline{Z}_{in}$ determines whether it's capacitive or inductive, let's examine the imaginary part first.

$$I_m(\overline{Z}_{in}(j\omega_s)) = \omega_s L_r - \frac{1}{\omega_s C_r} + \frac{64N^4 R_L{}^2 L_m \omega_s}{\pi^4 \omega_s{}^2 L_m{}^2 + 64N^4 R_L{}^2} \qquad (2\text{-}18)$$

When $\omega_s<\omega_r$, the zero-crossing frequency of Im($\overline{Z}_{in}$) increases as the R_L decreases, leading to its boundary $\omega_s=\omega_r$. When $\omega_s>\omega_r$, the imaginary part is always positive. We can divide the DC characteristic diagram into three parts as shown in Fig 2.8 [6]. Since we already know that the circuit will operate in ZVS mode when $\overline{Z}_{in}$ is inductive, we define this certain area to be Region

2. Conversely, we define the area where $\overline{Z}_{in}$ is capacitive and the circuit operates in ZCS mode to be Region 1. As seen in Fig 2.8, Region 2 includes two different parts. One is the area where $\omega_1 < \omega_s < \omega_r$ and another one is $\omega_s > \omega_r$. The first area is labeled as Region 2.1, and the second one is Region 2.2.

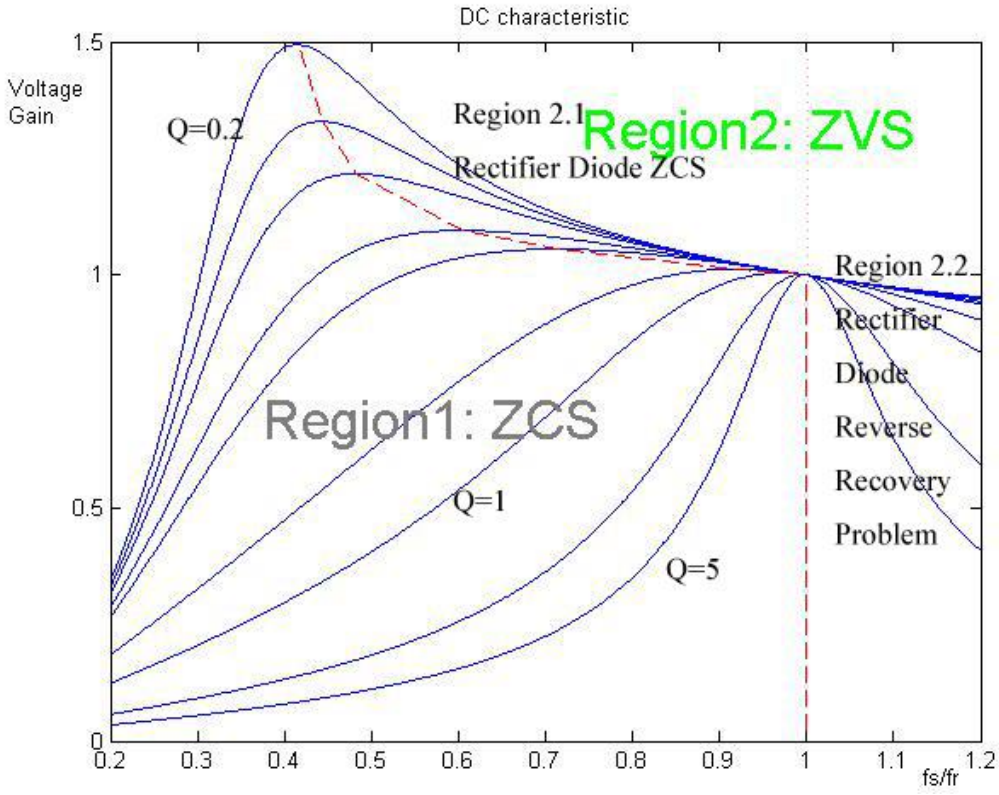

Fig 2.8 operating regions of LLC resonant converters

Because LLC resonant converters operate in a high-frequency mode, MOSFETs are widely used. As we have discussed, when using MOSFETs, the circuit should operate in a ZVS mode to minimize the power loss during switching. Thus, the LLC resonant converter should operate in Region 2, instead of Region 1 [7].

When $\omega_s < \omega_1$, the converter will always operate in the ZCS mode. While $\omega_s > \omega_r$, the converter will always operate in the ZVS mode. When $\omega_1 < \omega_s < \omega_r$, the operation depends on the

value of the load. Thus, we need to know the value of the load for the boundary between the ZVS and ZCS modes. Letting Im($\overline{Z}_{in}$)=0, we obtain:

$$\omega_s L_r - \frac{1}{\omega_s C_r} + \frac{64N^4 R_L^2 L_m \omega_s}{\pi^4 {\omega_s}^2 L_m^2 + 64N^4 {R_L}^2} = 0 \qquad (2\text{-}19)$$

Define

$$R_{Lb} = \frac{\pi^2 h Z_r k}{8N^2} \sqrt{\frac{1-k^2}{(1+h)k^2 - 1}} \qquad (2\text{-}20)$$

When $R_L > R_{Lb}$, the converter operates in the ZVS mode, where $k = \omega_s / \omega_r$. It can be seen in Fig 2.9 that $R_{Lb} = 0$ when $\omega_s > \omega_r$, which means that the converter will always operate in the ZVS mode. When $\omega_1 < \omega_s < \omega_r$, a higher switching frequency makes it easier for the converter to realize ZVS mode.

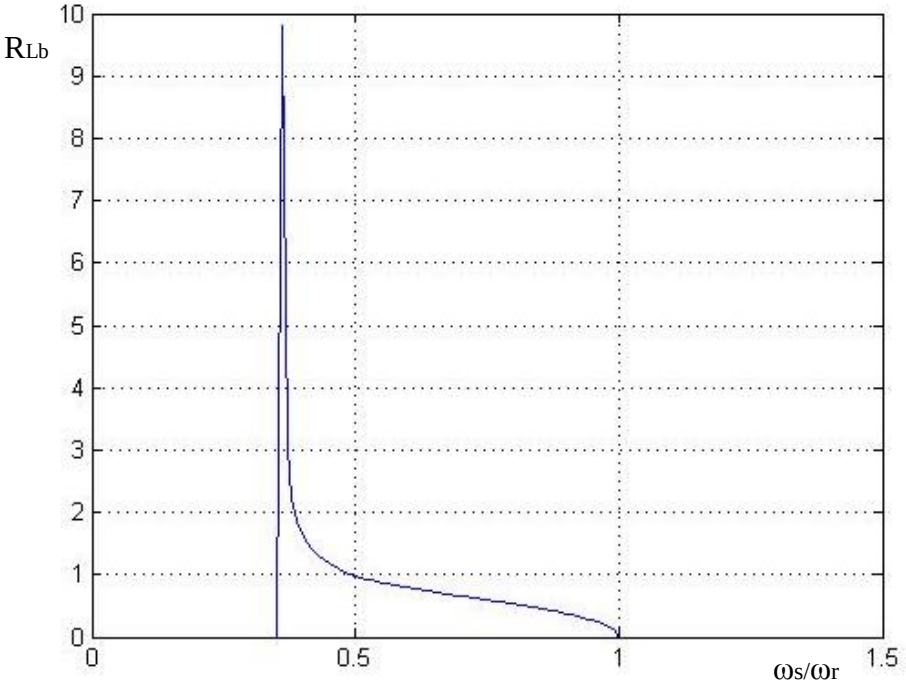

Fig 2.9 The relationship between R_{Lb} and k

When the converter is operating, the ideal status for the rectifier diodes is that there are not any reverse voltage oscillations. Because the converter operates in a high-frequency mode, the

distributed inductance of the secondary side (transformer's leakage inductance, line inductance) cannot be ignored. In Region 2.2, when D2 is on, D1 is reverse biased. The electric charge on the junction capacitance cannot be released instantly, which means D1 keeps conducting. However, at this time, D2 has already been turned-on, leaving a reverse recovery current flow in D1, causing a voltage oscillation across D1. While, in Region 2.1, before the diode D2 is turned on, the current in D1 has already reached zero, which means the diode has restored its reverse blocking capability. To better illustrate the differences between these two circumstances, simulation software SIMPLIS was used to generate simulated waveform results for these two regions. The SIMPLIS circuit is shown in Fig 2.10.

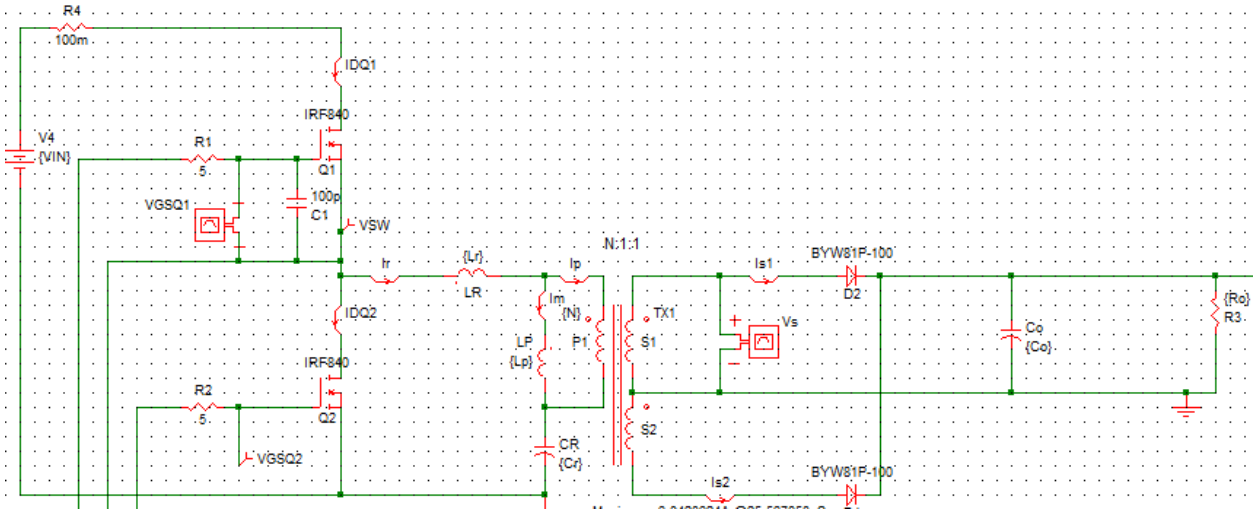

Fig 2.10 Simulation of an LLC resonant converter in SIMPLIS

In Fig 2.11, the case where the current flows through the two diodes D1 and D2 is presented. In Fig 2.11(a), the current flows through D1 and D2 share no overlapped area realizing a lower power loss operating mode. On contrary, the current waveform in Fig 2.11(b) tells us when D1 is turned on, D2 is still conducting. Thus, Region 2.1 has lower operating loss than Region 2.2.

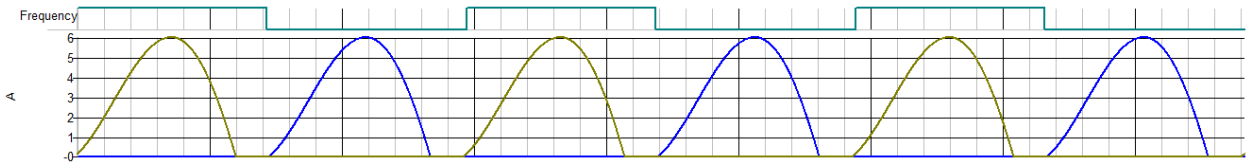

Fig 2.11 (a). Current waveform in D1 and D2 in Region 2.1

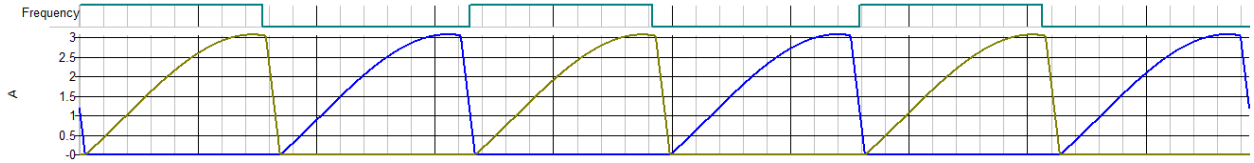

Fig 2.11 (b). Current waveform in D1 and D2 in Region 2.2

Due to the power loss caused by the reverse recovery, the ideal operating region is Region 2.1, not Region 2.2.

2-4. Operating process analysis for the LLC resonant converter

In this section, we make the following assumptions: V_{in} is constant, C_f is large enough to fix V_o at a constant value, and L_m is large enough to let the resonant tank complete a full resonant period.

As discussed earlier, the LLC resonant converter is a multi-resonant converter since the resonant frequency in different time intervals are different. Thus, the waveform should be divided into clearly two time intervals. The corresponding waveform of each component is shown in Fig 2.12.

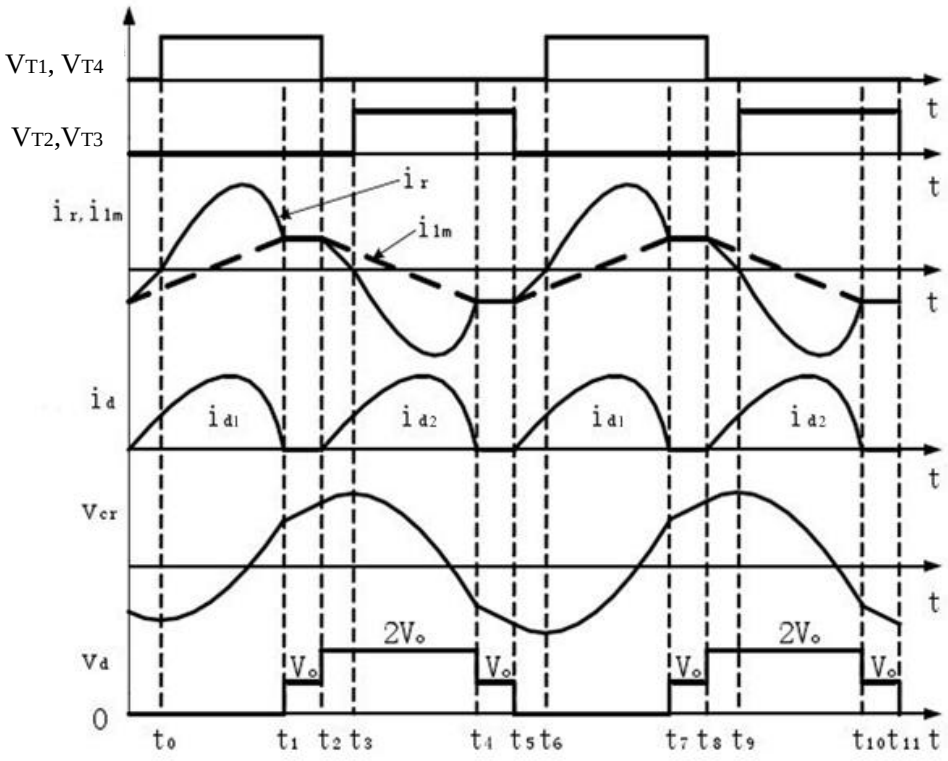

Fig 2.12 waveform during operating [3]

The whole operating process can be divided into six different stages [8] [9], which are shown in Fig 2.13. In these stages, t0 is the time when the current flowing through the resonant inductor L_r reaches 0 A. The current flow through L_m equals that through L_r at t1. The resonant current starts to decrease at t2. At t3, the resonant current reaches 0 A. The current flow through L_m equals that through L_r (negative value) at t4 and starts to increase at t5. At t6, the full resonant period is complete.

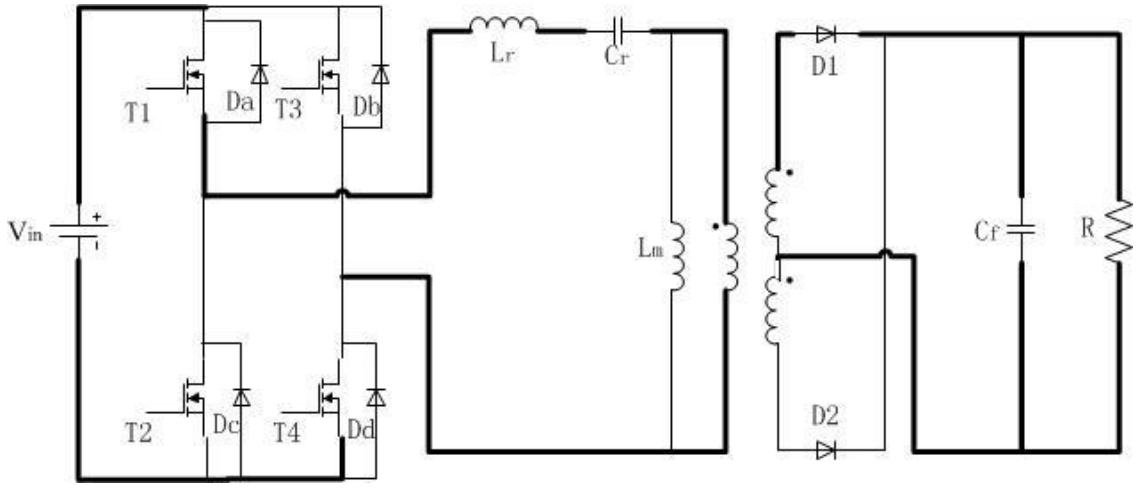

Fig 2.13(a). t0 to t1

Stage 1(t_0 to t_1): At t_0, T1 and T4 are turned-on, the resonant current flows through T1 and T4. Because before t_0, Da and Dd were on, it's a ZVS process. Since the voltage between the two poles of the secondary side of the transformer is positive, D1 is turned-on, supplying power to the load. During this period of time, the voltage across L_m is fixed at a constant value of NV_o. Thus, i_{Lm} increases linearly and Lm doesn't participate in the resonant process. The resonant frequency is f_r ($f_r = \frac{1}{2\pi\sqrt{L_r C_r}}$). Applying KCL and KVL, we can calculate the resonant current i_r and the voltage across the resonant capacitor C_r. In the following stages, KVL and KCL are utilized to calculate i_r and v_{cr} to verify the waveform in Fig 2.12. Also, the equations are preparation for the small signal modeling in the next chapter. For stage 1,

$$\begin{aligned} i_r(t) &= \frac{V_{in} - NV_o + V_{crm}}{Z_r} \sin\omega_r(t - t_0) \\ v_{cr}(t) &= V_{in} - NV_o - (V_{in} - NV_o + V_{crm}) \cos\omega_r(t - t_0) \end{aligned} \tag{2-21}$$

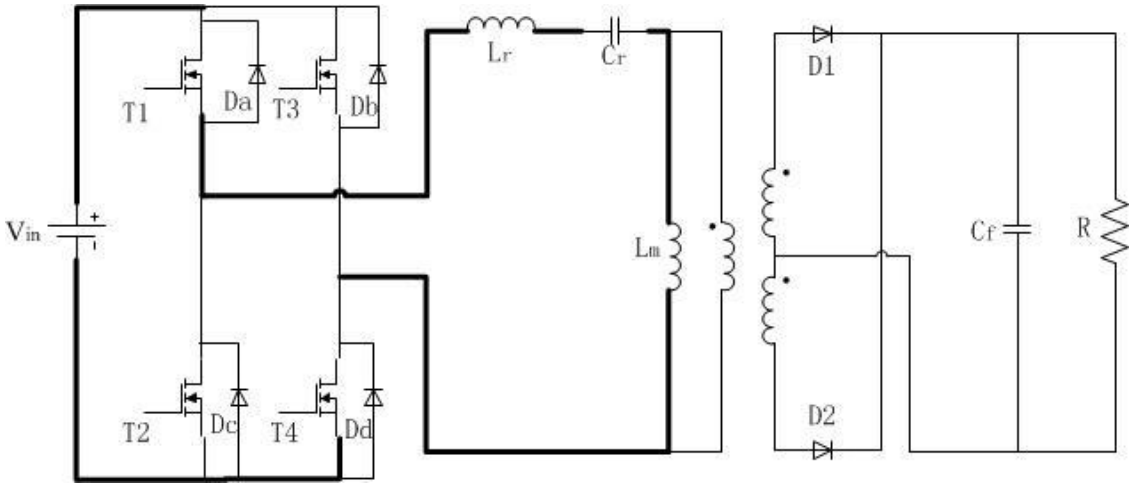

Fig 2.13 (b). t1 to t2

Stage 2(t_1 to t_2): when time reaches t1, $i_r=i_{Lm}$, due to KCL we know that the current flow into the primary side of the transformer is 0 A. So, there is no power transferred to the secondary side of the transformer. The voltage across L_m is no longer fixed at a certain value, and L_m will participate in the resonance in the second time interval. Because L_m is normally very large, we can assume that the resonant capacitor is charged constantly and its voltage increases linearly. (Im is the maximum value of the resonant current and the resonant frequency is f_1) The equations for this stage are

$$\begin{aligned} t_2 - t_1 &= \frac{T_s - T_r}{2} \\ i_r(t) &= I_m \\ v_{cr}(t) &= v_{cr}(t_1) + \frac{I_m}{C_r}(t - t_1) \end{aligned} \tag{2-22}$$

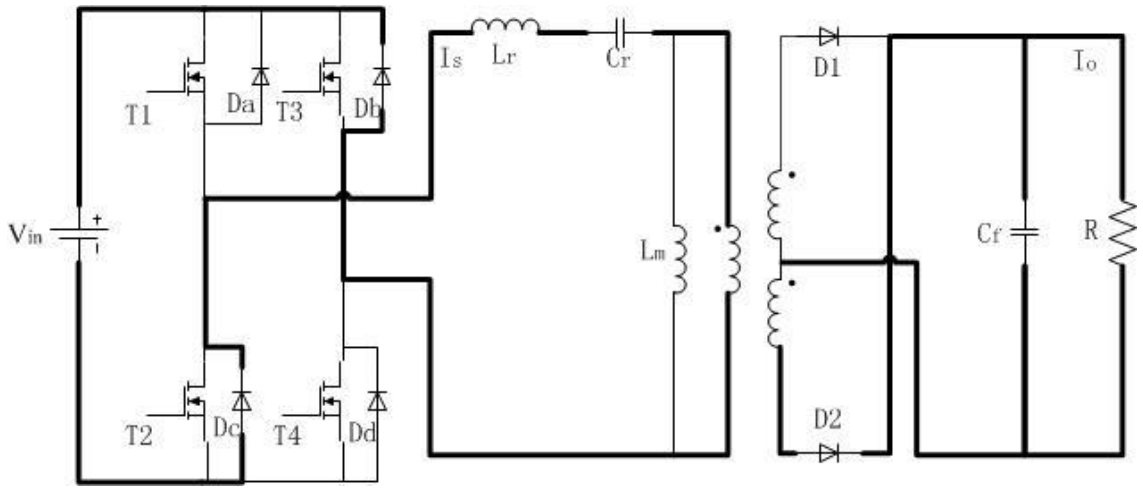

Fig 2.13 (c). t2 to t3

Stage 3(t_2 to t_3): At t_2, T1 and T4 are turned-off, Db and Dc turn on. As a result, the voltage across the primary side of the transformer is negative, turning on the diode D2. The voltage across L_m is fixed at $-NV_o$. Now, L_m is no longer part of the resonant tank. Its current decreases linearly. The resonant frequency of this period is f_r. The equations for this stage are

$$i_r(t) = I_m \cos \omega_r (t - t_2) \frac{V_{in} - NV_o + V_{cr}(t_2)}{Z_r} \sin \omega_r (t - t_2)$$
$$v_{cr}(t) = -V_{in} + NV_o + (V_{in} - NV_o + V_{cr}(t_2)) \cos \omega_r (t - t_2) + Z_r I_m \sin \omega_r (t - t_2) \quad (2\text{-}23)$$

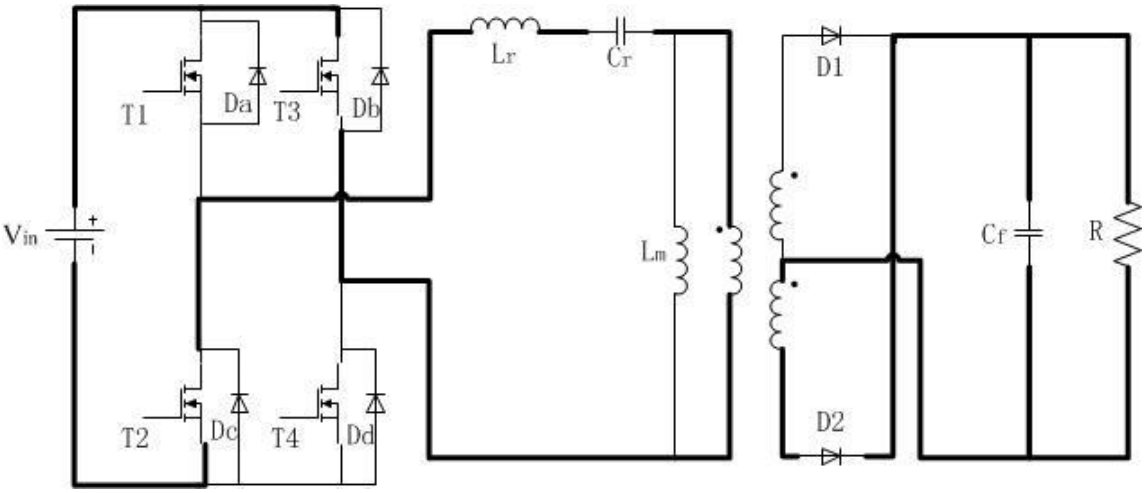

Fig 2.13 (d). t3 to t4

Stage 4(t_3 to t_4): At t_3, T2 and T4 are turned on. Because Db and Dc were on, this is a ZVS turn on. The voltage across the secondary side of the transformer is negative, and D2 continues to conduct. The voltage across L_m decreases linearly. The equations for this stage are

$$i_r(t) = -\frac{V_{in} - NV_o + V_{cr}(t_3)}{Z_r}\sin\omega_r(t-t_3)$$
$$v_{cr}(t) = -V_{in} + NV_o + (V_{in} - NV_o + V_{cr}(t_3))\cos\omega_r(t-t_3) \quad (2\text{-}24)$$

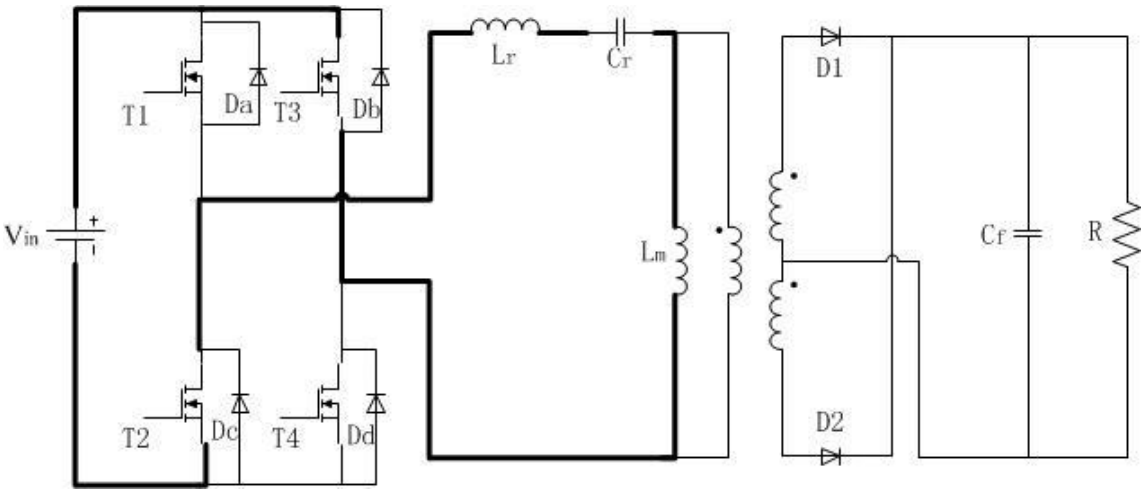

Fig 2.13 (e). t4 to t5

Stage 5(t_4 to t_5): At t_4, the current through Lm reaches -Im. There is no power flowing into the secondary side of the transformer. The equations for this stage are

$$t_5 - t_4 = \frac{T_s - T_r}{2}$$
$$i_r(t) = -I_m \quad (2\text{-}25)$$
$$v_{cr}(t) = v_{cr}(t_4) - \frac{I_m}{C_r}(t-t_4)$$

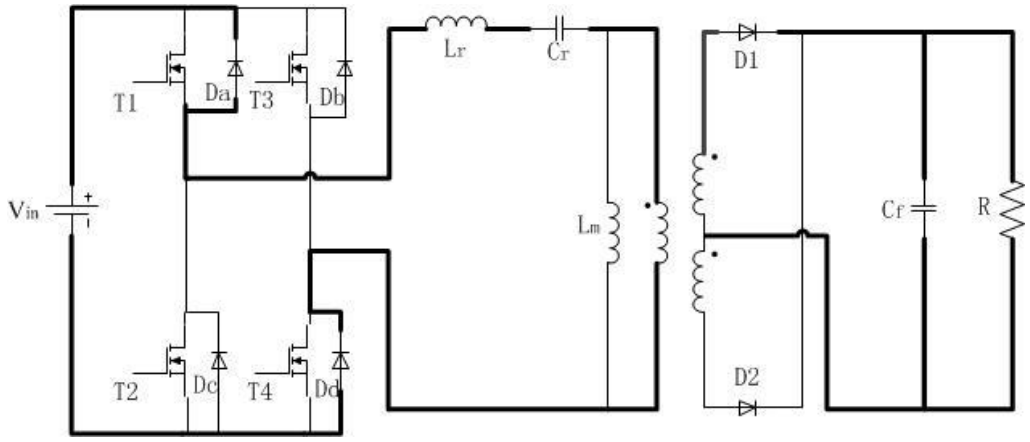

Fig 2.13 (f). t5 to t6

Stage 6(t_5 to t_6): T2 and T3 are turned-off, and Da and Dd turn on. The current through L_m increases linearly. The equations for this stage are

$$i_r(t) = -I_m \cos\omega_r(t-t_5) \frac{V_{in} - NV_o - V_{cr}(t_5)}{Z_r} \sin\omega_r(t-t_5)$$
$$v_{cr}(t) = V_{in} - NV_o - (V_{in} - NV_o - V_{cr}(t_5))\cos\omega_r(t-t_5) - Z_r I_m \sin\omega_r(t-t_5) \quad (2\text{-}26)$$

In an ideal situation, there are no DC components in the resonant current and resonant voltage. Thus $v_{cr}(t0) = -v_{cr}(t3) = v_{crm}$. Substituting this equation to (2-21) and (2-23), we can get:

$$v_{cr}(t2) = v_{cr}(t1) + \frac{I_m}{C_r}(t2-t1) = v_{cr}(t1) + \frac{I_m}{C_r}\frac{T_s - T_r}{2} \quad (2\text{-}27)$$

Because $v_{cr}(t1) = V_{in} - NV_o - (V_{in} - NV_o + V_{crm})\cos\omega_r(t1-t0)$ (2-28)

After substituting (2-28) into (2-27), and applying KVL due to the assumption that $i(t1) = i(t2) = I_m$, we can get

$$i(t1) = \frac{V_{in} - NV_o + V_{crm}}{Z_r} \sin\omega_r(t-t_o) = i(t2) \quad (2\text{-}29)$$

Substitute (2-29) to the conclusion of (2-21), we obtain:

$$i(t1) * Z_r = (V_{in} - NV_o + V_{crm}) \sin\omega_r(t-t0) \quad (2\text{-}30)$$

Because the characteristic impedance $Z_r = \frac{1}{\omega_r C_r}$, while the impedance of Cr at resonant frequency is $-j\frac{1}{\omega_r C_r}$. (2-30) can be converted into the voltage across the Cr at time t2 as $(V_{in} - NV_o + V_{crm})\cos\omega_r(t - t0)$. Thus, substituting v(t2) and (2-28) into (2-27) we can get

$$0 = NV_o - V_{in} - \frac{(T_s - T_r)I_m}{4NC_r} \tag{2-31}$$

$$V_o = \frac{V_{in}}{N} + \frac{(f_r - f_s)I_m}{4NC_r f_s f_r} \tag{2-32}$$

From the operating process we can see that there is no power switching during stages b and e, which is the main reason influencing the efficiency of the circuit. Also, from (2-28) we can see when V_o is fixed, V_{in} and T_s are negatively correlated. In other words, when the output voltage is higher, the efficiency becomes larger.

In this chapter, we compared two commonly used semi-conductor switches MOSFETs and IGBTs at first. After analyzing their features, we picked MOSFETs as the switches of this LLC resonant converter. Subsequently, we studied the LLC resonant converter in separated stages and obtained its large signal model and the voltage ratio of the input and output voltages. As a result, by utilizing MATLAB, we determined the operating region of the converter. And finally, based on the chosen operating region, we analyzed the different stages and obtained the expression of the output voltage and learned more about LLC resonant converter's features. In order to construct a stable LLC resonant converter, we also have to obtain its small signal model to analyze its stability and characteristic. This part will be discussed in the next chapter.

CHAPTER 3. Small signal modeling for LLC resonant converters

The small signal model of a SMPS system can represent the behavior of the converter near its equilibrium or stable operating point. In this chapter, several commonly used methods are introduced. Later the method of extended describing function is presented and utilized to model the LLC resonant converter. At last, the stability of the system is checked by utilizing computer program developed in MATLAB.

3-1. Commonly used methods for small signal modeling

For switching power supply control, it's often not easy to determine a small signal model in the presence of non-linear properties [10], [11], [12]. It shows the non-linearly property for two reasons:

1) switching process: When MOSFETs are turned on and off at different times, the circuit topology changes. The state variable equations describing the circuit operation vary periodically.

2) components: Component non-linearity results from the saturation of magnetic cores.

There are several ways to develop a small signal model.

- State-space averaging method: Ignore the higher order terms in one period when the switching frequency is high. Use a linear time invariant (LTI) state equation to approximate the operation of the SMPS system.
- Generalized averaging method: Based on a harmonic balance, Fourier analysis can be used on each state variable to derive a small signal model.
- Discrete time-domain simulation method: Use the state-space method to infer piecewise linear equations and non-linear differential equations.

Dr. Eric X.Yang has developed a small signal modeling process based on the generalized averaging method [10]. For this method, apply Fourier analysis to each state variable and obtain a small signal model using the harmonic balance method, which was proposed by J. Groves [11]. This modeling method is referred to as Extended Describing Function and can be utilized in the analysis and modeling of resonant and multi-resonant converters.

3-2. Extended describing function

For DC/DC converters, an equivalent system contains three individual input variables known as the controlling input (switching frequency), input voltage (Vg) and loading current (Io). Variables $\hat{V}_o(s), \hat{\omega}_s(s), \hat{V}_g(s), \hat{i}_o(s)$ stands for the small signal perturbation values. The system can be described by the following equivalent model:

$$\hat{V}_o(s) = G_{vw_s}(s)\hat{\omega}_s(s) + G_{vg}(s)\hat{V}_g(s) + G_{vi}(s)\hat{i}_o(s) \qquad (3\text{-}1)$$

In this model, $G_{vw_s}(s) = \left.\frac{\hat{V}_o(s)}{\hat{\omega}_s(s)}\right|_{\substack{\hat{V}_g(s)=0 \\ \hat{i}_o(s)=0}}$; $G_{vg}(s) = \left.\frac{\hat{V}_o(s)}{\hat{V}_g(s)}\right|_{\substack{\hat{\omega}_s(s)=0 \\ \hat{i}_o(s)=0}}$; $G_{vi}(s) = \left.\frac{\hat{V}_o(s)}{\hat{i}_o(s)}\right|_{\substack{\hat{V}_g(s)=0 \\ \hat{\omega}_s(s)=0}}$,

stands for transfer function from switching frequency, input voltage and load current to the output voltage. A system model based on (3-1) is shown in Fig 3.1

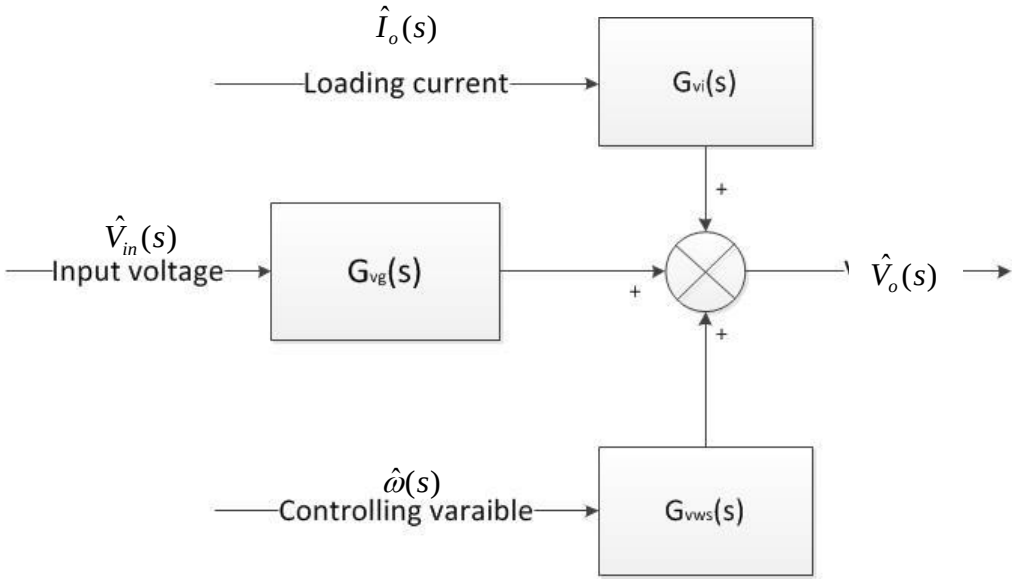

Fig 3.1 Small signal equivalent model

3-2-1 Defining extended describing function

The state equation of the converter system can be written as:

$$\begin{cases} \dot{x} = f(x,u,t) \\ y = g(x,u,t) \end{cases} \tag{3-2}$$

Under steady-state, the input u is a constant vector and the state trajectory is periodic over the switching period, T_s. Therefore, the state vector can be expanded into Fourier series:

$$x^{ss}(t) = \sum_{k=-\infty}^{\infty} X_k^{ss} e^{jk\omega_s t} \tag{3-3}$$

where

$$X_k^{ss} = \frac{1}{T_s}\int_0^{T_s} x^{ss}(t) e^{-jk\omega_s t} dt, \omega_s = \frac{2\pi}{T_s} \tag{3-4}$$

The superscript, ss, represents the steady-state operation.

Similarly, the nonlinear function defined in (3-2) can also be expanded into Fourier series under steady state operation:

$$f\left(x^{ss},U_o,t\right)=\sum_{k=-\infty}^{\infty}F_k^{ss}(X^{ss},U_o)e^{jk\omega_s t}dt \tag{3-5}$$

where

$$\begin{aligned} F_k^{ss}(X^{ss},U_o) &= \frac{1}{T_s}\int_0^{T_s} f(x^{ss}(t),U_o,t)e^{-jk\omega_s t}dt \\ X^{ss} &= (...,X_{-k}^{ss},...,X_0^{ss},...,X_k^{ss},...) \end{aligned} \tag{3-6}$$

The Fourier coefficient, $F_k^{ss}(X^{ss},U_o)$ is a function of the steady-state input, U_o, and all of the Fourier coefficients of $x^{ss}(t)$. Therefore, $F_k^{ss}(X^{ss},U_o)$ can be called a multi-variable describing function [10].

3-2-2 Review of Grove's Method [11]

As mentioned earlier, the extended describing function method is based on the harmonic balanced method proposed by J. Grove. Thus, a brief introduction of J. Groves method is necessary. His method is based on the Fourier analysis over the commensurate period [11]. The bridge that relates the state vector spectrum and the non-linear function spectrum (describing function terms) is harmonic balance. Thus, an equation can be derived as:

$$\sum_{l=-\infty}^{\infty} jl\omega_c X_l e^{jl\omega_c t} = \sum_{l=-\infty}^{\infty} F_l(X,U)e^{jl\omega_c t} \tag{3-7}$$

In (3-7), the term $e^{jl\omega_c t}$ are the same. Thus, to let the equation to be established, the Fourier coefficients of each term harmonics should be equal, which can be written as:

$$jl\omega_c X_l = F_l(X,U) \tag{3-8}$$

This procedure is called harmonic balance. Expanding by Taylor series, the equation can be written as:

$$jl\omega_c X_l = \sum_{m=-\infty}^{\infty} \frac{\partial F_l}{\partial X_l} X_l + \frac{\partial F_l}{\partial U_o} \hat{u} \tag{3-9}$$

If the partial derivatives are known and we limit the terms as a finite number from -H to H, then the small-signal spectrum X_l can be obtained. In this way, the system's small signal model can be derived. Nevertheless, J.Grove's method has some disadvantages. The harmonic balance method depends on knowing the information of every modulation frequency in order to obtain partial derivatives for calculating. Thus, this procedure is very complicated and inconvenient to use.

3-2-3 Extended describing function for multi-resonant converters

The nonlinear state equation for an LLC resonant converter is given in (3-2). Applying Fourier analysis to each side of the two equations yields:

$$\begin{cases} x(t) = \sum_{k=-\infty}^{\infty} X_k(t) e^{jk\omega_s t} \\ y(t) = \sum_{k=-\infty}^{\infty} Y_k(t) e^{jk\omega_s t} \\ f(x,u,t) = \sum_{k=-\infty}^{\infty} F_k(X,U) e^{jk\omega_s t} \\ g(x,u,t) = \sum_{k=-\infty}^{\infty} G_k(X,U) e^{jk\omega_s t} \end{cases} \tag{3-10}$$

As mentioned, defining $F_k(X,U)$ and $G_k(X,U)$ to be describing functions of the state variables and output variables.

$X = \{\cdots, X_{-k}, \cdots, 0, \cdots, X_k, \cdots\}^T, U = \{U_o\}, Y = \{Y_o\}$ stand for state variables $\dot{x}$, u is the input voltage, and y is the output DC current. Here we should note that U and Y only have DC

components. For each switching period, voltage across L_r and C_r is reset to 0 V along with the current, which makes $\frac{dx}{dt} = 0$.

Thus, the 0th order of the describing function $F_k(X,U)$ is 0.

$$F_0(X,U) = \frac{1}{T_s}\int_0^{Ts} f(x,u,t)dt = 0 \tag{3-11}$$

Now take derivatives of each side of equation (3-10):

$$\dot{x}(t) = \sum_{k=-\infty}^{\infty} \dot{X}_k(t)e^{jk\omega_s t} + \sum_{k=-\infty}^{\infty} jK\omega_s X_k(t)e^{jk\omega_s t} \tag{3-12}$$

Here, J. Grove's harmonic balance method is utilized. Substituting (3-12) back into (3-2), we obtain:

$$\begin{cases} \dot{X}_k(t) + jk\omega_s X_k(t) = F_k(X,U) \\ Y_o = G_o(X,U) \end{cases} \tag{3-13}$$

Equation (3-13) is actually the frequency expression for (3-2), when the system is stable,

$X_k(t) = X_k{}^{ss}, \dot{X}_k(t) = 0,$

Equation (3-13) can be written as

$$\begin{cases} jk\omega_s X_k(t) = F_k^{ss}(X^{ss},U_o) \\ Y_0 = G_0^{ss}(X^{ss},U_0) \end{cases} \tag{3-14}$$

When there are small signal perturbations,

$$\begin{cases} X_k(t) = X_k{}^{ss} + \hat{X}_k \\ \omega_s = \Omega^{ss} + \hat{\omega}_s \\ u = U_o + \hat{u} \\ y = Y_o + \hat{y}_o \end{cases} \tag{3-15}$$

If we make a substitution into (3-14), expand describing functions $F_k(X,U)$ and $G_k(X,U)$

into Taylor series, ignore partial derivatives higher than second order and cancel the stable components, we can get:

$$\begin{cases} \dot{\hat{X}}_k^{ss} + jk\hat{\omega}_s X_k^{ss} + jk\Omega_s \hat{x}_k = \sum_{m=-H}^{H} \frac{\partial F_k^{ss}}{\partial X_m^{ss}} \hat{x}_m + \frac{\partial F_k^{ss}}{\partial U_0} \hat{u} \\ \hat{y}_0 = \sum_{m=-H}^{H} \frac{\partial G_0^{ss}}{\partial X_m^{ss}} \hat{x}_m + \frac{\partial G_0^{ss}}{\partial U_0} \hat{u} \end{cases} \tag{3-16}$$

From these equations, if the variable is only ω_s, then the system small signal model can be written as:

$$\begin{cases} \dot{\hat{X}}_k^{ss} + jk\hat{\omega}_s X_k^{ss} + jk\Omega_s \hat{x}_k = \sum_{m=-H}^{H} \frac{\partial F_k^{ss}}{\partial X_m^{ss}} \hat{x}_m \\ \hat{y}_0 = \sum_{m=-H}^{H} \frac{\partial G_0^{ss}}{\partial X_m^{ss}} \hat{x}_m \end{cases} \tag{3-17}$$

This is the familiar form $\begin{cases} \dot{\hat{x}} = A_s \hat{x} + B_s \hat{\omega}_s \\ \hat{y}_o = C_s \hat{x} \end{cases}$.

Here,

$$A_s = \begin{bmatrix} \frac{\partial F_{-H}^{ss}}{\partial X_{-H}^{ss}} + jH\Omega_s & \cdots & \frac{\partial F_{-H}^{ss}}{\partial X_m^{ss}} & \cdots & \frac{\partial F_{-H}^{ss}}{\partial X_H^{ss}} \\ \cdots & \cdots & & \cdots & \cdots \\ \frac{\partial F_m^{ss}}{\partial X_{-H}^{ss}} & \cdots & \frac{\partial F_m^{ss}}{\partial X_m^{ss}} - jm\Omega_s & \cdots & \frac{\partial F_m^{ss}}{\partial X_H^{ss}} \\ \cdots & \cdots & & \cdots & \cdots \\ \frac{\partial F_H^{ss}}{\partial X_{-H}^{ss}} & \cdots & \frac{\partial F_H^{ss}}{\partial X_m^{ss}} & \cdots & \frac{\partial F_H^{ss}}{\partial X_H^{ss}} - jH\Omega_s \end{bmatrix}$$

$$B_s = (jHX_{-H}^{ss}, ..., -jmX_m^{ss}, ..., -jHX_H^{ss})^T \tag{3-18}$$

$$C_s = (\frac{\partial G_o^{ss}}{\partial X_{-H}^{ss}}, ..., \frac{\partial G_o^{ss}}{\partial X_m^{ss}}, ..., \frac{\partial G_o^{ss}}{\partial X_H^{ss}})$$

If we examine the different states of the LLC converter, we can divide the whole switching

period into different pieces. Then,

$$\begin{cases} \dot{\hat{x}} = A_i \hat{x} + B_i u \\ \hat{y}_o = C_i \hat{x} + D_i u \end{cases} \quad T_{i-1} < t < T_i \tag{3-19}$$

$$F_k^{ss}(X^{ss}, U_o) = \frac{1}{T_s} \sum_{t=1}^{Q} \int_{T_{i-1}}^{T_i} \left[A_i x^{ss}(t) + B_i U_o \right] e^{-jk\omega_s t} dt \tag{3-20}$$

$$\frac{\partial F_k^{ss}(X^{ss}, U_o)}{\partial X_m^{ss}} = \frac{1}{T_s} \sum_{t=1}^{Q} \left\{ [A_i x^{ss}(T_i) + B_i U_o] e^{-jk\omega_s T} \frac{\partial T_i}{\partial X_m^{ss}} - [A_i x^{ss}(T_{i-1}) + B_i U_o] e^{-jk\omega_s T_{i-1}} \frac{\partial T_{i-1}}{\partial X_m^{ss}} + \int_{T_{i-1}}^{T_i} A_i \frac{\partial x^{ss}(t)}{\partial X_m^{ss}} e^{-jk\omega_s t} dt \right\} \tag{3-21}$$

Where Q stands for the numbers of pieces in one switching period.

As a result, $\frac{\partial x^{ss}}{\partial X_m^{ss}} = e^{jm\omega_s t}$ (3-22)

Assuming that the boundary condition is

$$h(T_i, x^{ss}, U_o) = A_{bi} x^{ss}(T_i) + B_{bi} T_i + C_{bi} U_o + D_{bi} > 0,$$

$$\frac{\partial T_i}{\partial X_m^{ss}} = -\frac{\frac{\partial h}{\partial X_m^{ss}}}{\frac{\partial h}{\partial T_i}} = \frac{-A_{bi} e^{jm\omega_s T_i}}{A_{bi}[A_i x^{ss}(T_i) + B_i U_o] + B_{bi}} \tag{3-23}$$

Due to equations (3-21), (3-22) and (3-23), we can get the small signal model of the system. We have introduced the basic method of Extended Describing Function in this section. Since Now we can derive an LLC resonant converter's small signal model if we know the linearized state equations for different operating stages. The next step is to calculate state equations of pieces of the linear network in one switching cycle.

3-3. Small signal modeling for the LLC resonant converter

In this section, we regard the perturbation of the load (state variable I_o) as the only perturbation in the converter. The equivalent series resistance (ESR) of the capacitor C_f would cause a voltage drop on the output variable V_o; thus, a low value of ESR is considered during the modeling process. We obtain 4 different modes of operation for the LLC converter which are shown in Fig 3.2 (a, b, c, d). Each mode corresponds to certain operating stages in Fig 2.13.

A piece-wise linearizated equation can be derived from the small signal modeling method described above.

In this section, we assume the input matrix $u=[V_{in}, I_o]^T$, output matrix $y=[V_o, I_g]^T$, Ig is the input current. State variables $x=[x_1, x_2, x_3, x_4]^T=[i_{L_r}\ -i_{L_m}, i_{L_m}, v_{C_r}, v_{C_f}]^T$.

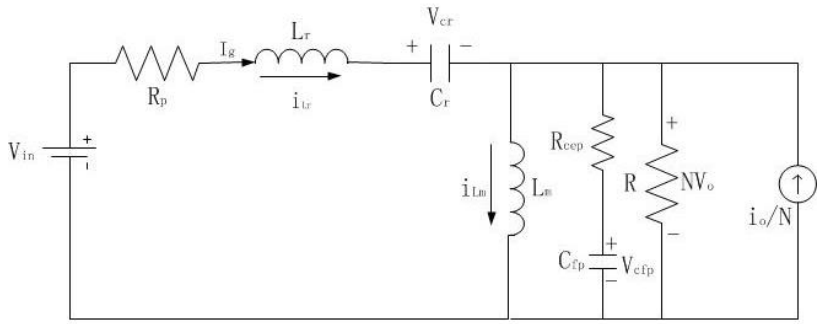

Fig 3.2 (a) mode a (stages 1&6)

Fig 3.2 (a) shows the equivalent circuit for topology “mode a” that stands for operating pieces of stage 1 and stage 6 in Chapter 2. In stage 1 and stage 6, power flows from the primary side to the secondary side. In Fig 3.2, all the components on the secondary side are referred to the primary side. C_{fp} represents the filter capacitor C_f on the primary side, R_{cep} represents the ESR value on the primary side and R represents the load resistance value R_L on the primary side.

Also, to introduce the variation of the load current i_o to the primaty side, a current source i_o/N is added to the circuit's primary side. Applying KCL and KVL to the circuit operating piece of mode a, we can obtain the equations for the state variables.

$$\begin{cases} L_r\dot{x}_1 + (L_r + L_m)\dot{x}_2 = -R_p(x_1 + x_2) - x_3 + V_{in} \\ \dot{x}_3 = \dfrac{1}{C_r}(x_1 + x_2) \\ (C_{fp} + \dfrac{R_{ce}C_{fp}}{R})\dot{x}_4 = x_1 - \dfrac{x_4}{R} + \dfrac{i_o}{N} \\ L_m\dot{x}_2 = x_4 + R_{cep}C_{fp}\dot{x}_4 \\ NV_o = R(x_1 - C_{fp}\dot{x}_4 + \dfrac{i_o}{N}) \\ I_g = x_1 + x_2 \end{cases} \tag{3-24}$$

Define $r = \dfrac{RR_{cep}}{R + R_{cep}} and, k = \dfrac{R}{R + R_{cep}}$ As a result:

$$A_1 = \begin{bmatrix} -\dfrac{r + R_p}{L_r} - \dfrac{r}{L_m} & -\dfrac{R_p}{L_r} & -\dfrac{1}{L_r} & -k(\dfrac{1}{L_r} + \dfrac{1}{L_m}) \\ \dfrac{r}{L_m} & 0 & 0 & \dfrac{k}{L_m} \\ \dfrac{1}{C_r} & \dfrac{1}{C_r} & 0 & 0 \\ \dfrac{k}{C_{fp}} & 0 & 0 & -\dfrac{k}{RC_{fp}} \end{bmatrix} \qquad C_1 = \begin{bmatrix} \dfrac{r}{N} & 0 & 0 & \dfrac{k}{N} \\ 1 & 1 & 0 & 0 \end{bmatrix}$$

$$B_1 = \begin{bmatrix} \dfrac{1}{L_r} & 0 & 0 & 0 \\ -\dfrac{r}{N}(\dfrac{1}{L_r} + \dfrac{1}{L_m}) & \dfrac{r}{NL_m} & 0 & \dfrac{k}{NC_{fp}} \end{bmatrix}^T \qquad D_1 = \begin{bmatrix} 0 & \dfrac{r}{N^2} \\ 0 & 0 \end{bmatrix}$$

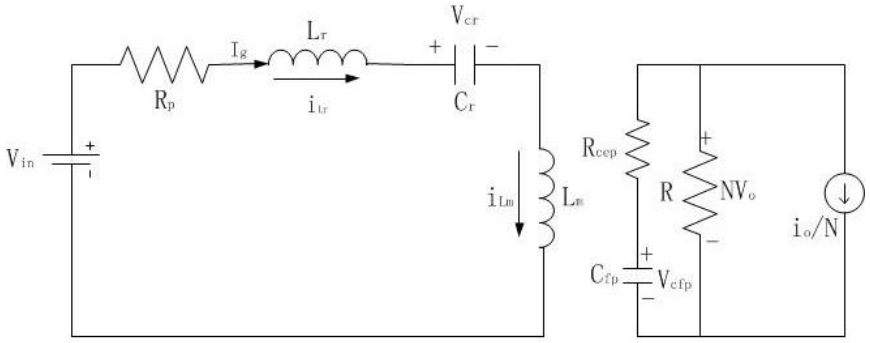

Fig 3.2 (b) mode b (stage2)

In mode b, there is no power flow from the primary side to the secondary side. Thus, the components in the secondary side are separated from those in the primary side, which means $i_{Lr} = i_{Lm}$ Applying KVL and KCL to the circuit, the equations for mode b can be derived as:

$$\begin{cases} \dot{x}_1 = 0 \\ \dot{x}_2 = -\dfrac{R_p}{L_r + L_m} x_2 - \dfrac{1}{L_r + L_m} x_3 + \dfrac{V_{in}}{L_r + L_m} \\ \dot{x}_3 = \dfrac{1}{C_r} x_2 \\ \dot{x}_4 = -\dfrac{k x_4}{R C_{fp}} + \dfrac{k i_o}{N C_{fp}} \\ V_o = \dfrac{k}{N} x_4 + \dfrac{r}{N^2} i_o \\ I_g = x_2 \end{cases} \tag{3-25}$$

$$A_2 = \begin{bmatrix} 0 & 0 & 0 & 0 \\ 0 & -\dfrac{R_p}{L_r + L_m} & -\dfrac{1}{L_r + L_m} & 0 \\ 0 & \dfrac{1}{C_r} & 0 & 0 \\ 0 & 0 & 0 & -\dfrac{k}{R C_{fp}} \end{bmatrix} \qquad C_2 = \begin{bmatrix} 0 & 0 & 0 & \dfrac{k}{N} \\ 1 & 1 & 0 & 0 \end{bmatrix}$$

$$B_2 = \begin{bmatrix} 0 & \frac{1}{L_r + L_m} & 0 & 0 \\ 0 & 0 & 0 & \frac{k}{NC_{fp}} \end{bmatrix}^T \qquad D_2 = \begin{bmatrix} 0 & \frac{r}{N^2} \\ 0 & 0 \end{bmatrix}$$

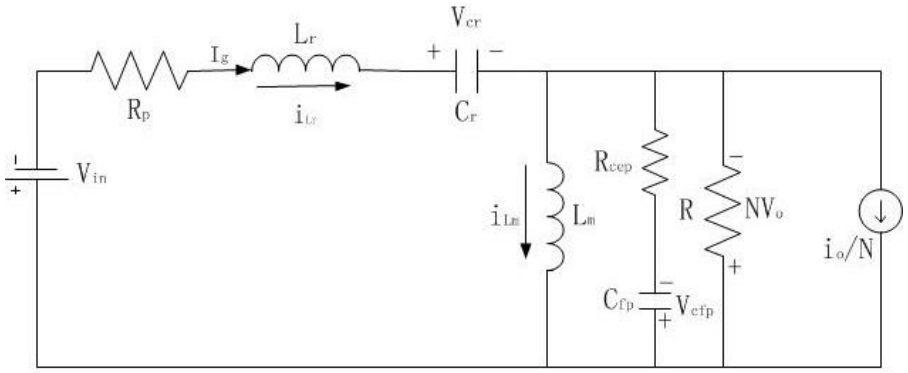

Fig 3.2 (c) mode c (stages 3&4)

Compared to stage 1 and stage 6, mode c has the same topology mode that shows the power flows from the primary side to the secondary side. But the difference between mode a and mode c is that Vin, Vo and the voltage across the filter capacitor has the opposite polarity. Thus, the matrices can be easily derived.

For mode c:

$$A_3 = \begin{bmatrix} -\frac{r+R_p}{L_r} - \frac{r}{L_m} & -\frac{R_p}{L_r} & -\frac{1}{L_r} & -k(\frac{1}{L_r} + \frac{1}{L_m}) \\ \frac{r}{L_m} & 0 & 0 & -\frac{k}{L_m} \\ \frac{1}{C_r} & \frac{1}{C_r} & 0 & 0 \\ -\frac{k}{C_{fp}} & 0 & 0 & -\frac{k}{RC_{fp}} \end{bmatrix} \qquad C_3 = \begin{bmatrix} -\frac{r}{N} & 0 & 0 & \frac{k}{N} \\ -1 & -1 & 0 & 0 \end{bmatrix}$$

$$B_3 = \begin{bmatrix} -\frac{1}{L_r} & 0 & 0 & 0 \\ \frac{r}{N}\left(\frac{1}{L_r}+\frac{1}{L_m}\right) & -\frac{r}{NL_m} & 0 & \frac{k}{NC_{fp}} \end{bmatrix}^T \qquad D_3 = \begin{bmatrix} 0 & \frac{r}{N^2} \\ 0 & 0 \end{bmatrix} \qquad (3\text{-}26)$$

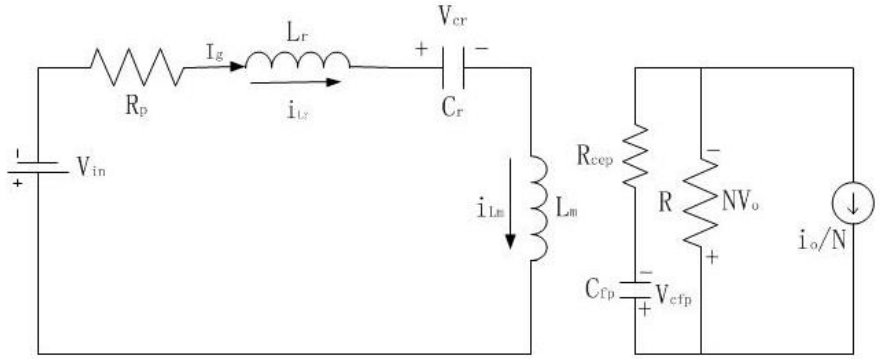

Fig 3.2 (d) mode d (stage 5)

Matrices for mode d can be derived by changing the direction of Vin, Vo and Vcfp of matrices for mode b. In other words, mode c and mode a share the same eigenvalues, while mode b and mode d share the same eigenvalues. For mode d:

$$A_4 = \begin{bmatrix} 0 & 0 & 0 & 0 \\ 0 & -\frac{R_p}{L_r+L_m} & -\frac{1}{L_r+L_m} & 0 \\ 0 & \frac{1}{C_r} & 0 & 0 \\ 0 & 0 & 0 & -\frac{k}{RC_{fp}} \end{bmatrix} \qquad C_4 = \begin{bmatrix} 0 & 0 & 0 & \frac{k}{N} \\ -1 & -1 & 0 & 0 \end{bmatrix}$$

$$B_4 = \begin{bmatrix} 0 & -\frac{1}{L_r+L_m} & 0 & 0 \\ 0 & 0 & 0 & \frac{k}{NC_{fp}} \end{bmatrix}^T \qquad D_2 = \begin{bmatrix} 0 & \frac{r}{N^2} \\ 0 & 0 \end{bmatrix} \qquad (3\text{-}27)$$

Now we have information of four operating pieces in one switching period. As introduced

earlier that with state equations in each of these pieces, equation (3-21) can be derived by substituting these state equations into Ai, Bi, Ci and Di (i=1,2,3,4). Note that this procedure is complicated so a computer program based on MATLAB should be utilized. The software package for extended describing function can be found in dissertation of Dr. Eric X. Yang[10].

3-4. Stability analysis

The block diagram of the LLC converter controlled system is shown in Fig 3.3:

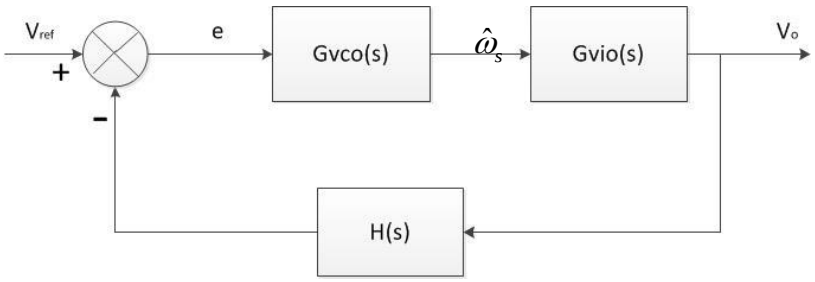

Fig 3.3 Block diagram for the control strategy

In Fig 3.3, Gvio is the transfer function of the resonant tank. Also, when adding the feedback to the system, the comparison result of the output voltage and the reference voltage has to be converted into a varying modulating frequency. Thus, Gvco represents the transfer function of the voltage controlled oscillator (VCO), and H(s) is the sampling circuit's transfer function. In an ideal situation, VCO is assumed as a linear function whose input is the voltage control signal Vc and the output is the switching frequency f.

In order to illustrate the stability of the feedback controlled LLC resonant converter, Matlab is used to calculate the small signal model of the converter and utilize control theory to test the stability of it. In the simulated system, parameters utilized are shown as follows:

$$V_{in} = 40\,V; N = 4; h = L_m / L_r = 6;$$
$$f_r = 80\,kHz; C_f = 20\,uF; r_p = r_{ce} = 0.01\,\Omega;$$
$$L_r = 7.8\,uH; L_m = 52.5\,uH; C_r = 470\,nF$$

After substituting parameters into the small signal model which was proposed in the former section, state space matrices A,B,C and D were calculated in Matlab and the transfer function was derived as well. The MATLAB file is given in Appendix A.

The transfer functions for each block shows as follows:

$$H(s) = \frac{5}{11}; G_{vco}(s) = 20*10^3$$

$$A = \begin{bmatrix} -2576.05225965017 & -1288.65979381443 & -128865.979381443 & -128739.246583573 \\ 190.288867331148 & 0 & 0 & 19028.8867331149 \\ 2127659.57446809 & 2127659.57446809 & 0 & 0 \\ 49950.8276744265 & 0 & 0 & -4917.23255735162 \end{bmatrix}$$

$$B = \begin{bmatrix} 128865.979381443 & -1287.39246583573 \\ 0 & 190.288867331149 \\ 0 & 0 \\ 0 & 49950.8276744265 \end{bmatrix}$$

$$C = \begin{bmatrix} 0.00999 & 0 & 0 & 0.999 \\ 1 & 1 & 0 & 0 \end{bmatrix}$$

$$D = \begin{bmatrix} 0 & 0.01 \\ 0 & 0 \end{bmatrix}$$

$$G_{vio}(s) = \frac{0.01s^4 + 4.996*10^4 s^3 + 2.8*e^9 s^2 + 1.369e^{16} s - 389.25}{s^4 + 7.49*10^3 s^3 + 2.81*10^{11} s^2 + 1.4*10^{15} s + 2.69*10^{20}}$$

In order to test the stability of the system. Bode plot of the transfer function was plotted in Fig 3.4. The system is a high order system that has several zeros and poles, which are plotted in Fig. 3.5. In this figure, the zeros are relatively closer to the original. For verifying the stability,

a Nyquist diagram is necessary. The magnitude phase curve of the system open loop transfer function is shown in Fig. 3.6.

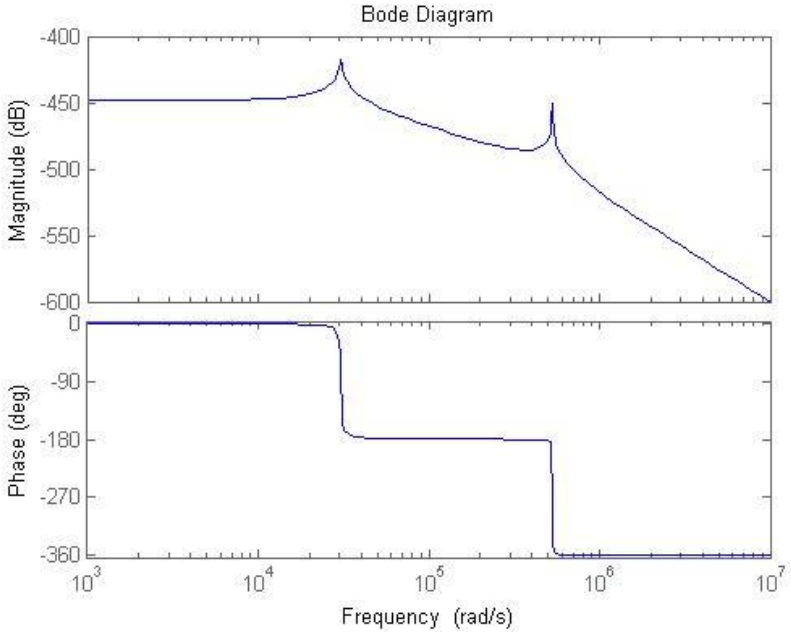

Fig 3.4 Bode plot of the open loop transfer function

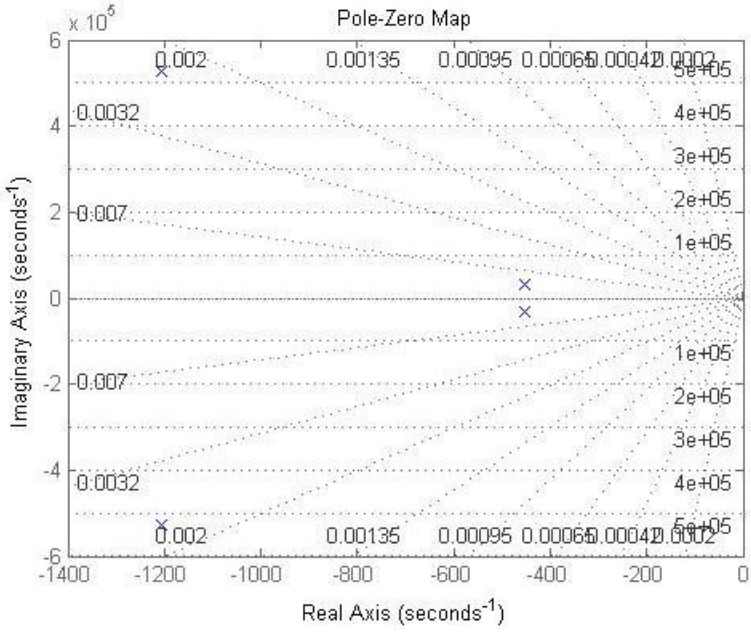

Fig 3.5 Poles and zeros of the open loop transfer function

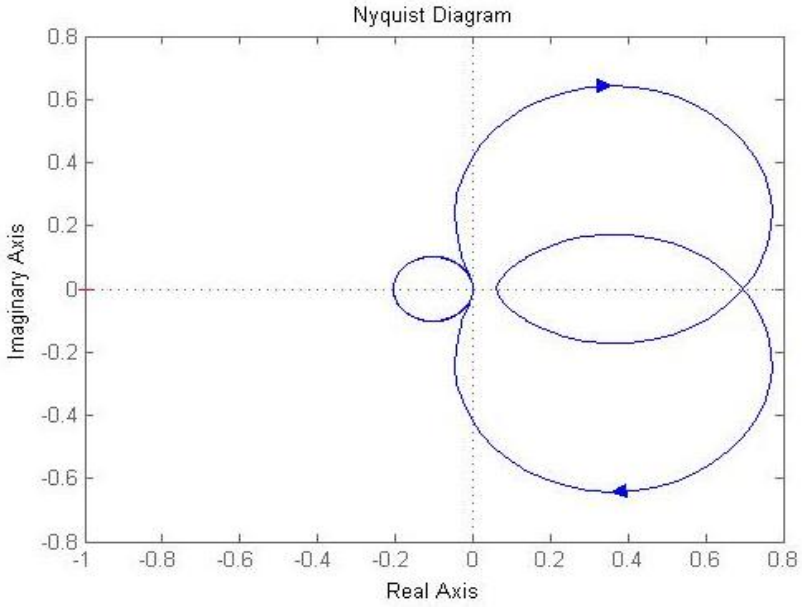

Fig 3.6 Open loop magnitude-phase curve

We use the Nyquist stability criterion to check stability. The number of poles of open-loop transfer function in the RHP is P=0. Also, the number of times that the magnitude-phase curve circles (-1,j0) in the counterclockwise direction is N=0. Thus, number of the closed-loop function's positive real eigenvalue is Z=0. As a result, the system is stable.

In this chapter, the introduction of the extended describing function is illustrated firstly. Because the method of extended describing function requires the piece-wise linear functions of each operation mode, the linearized matrices for Region 2.1 were presented. Finally, by utilizing the method of extended describing function, the stability of the system was verified. Now the design of a prototype converter is described in Chapter 4.

CHAPTER 4. Circuit Design and Construction

In this chapter we select the parameters for the prototype converter. And then the process of constructing an LLC resonant converter is illustrated. At last, the appropriate analog-control chip is utilized to control the output voltage.

4-1. Design of the LLC resonant converter

The design parameters for the converter are:

Input voltage: 35~40 V;

Output voltage: 10 V(+/-5%);

Rated output current: 1 A;

Rated power: 40 W;

Switching frequency range: 60 kHz~80 kHz.

In this circuit, the first parameter to be selected is the turns ratio of the transformer. Since the input voltage varies between 35 V to 40 V, and the output voltage is about 10V, the ratio of the input voltage to output voltage is 3.5 to 4. Since the voltage gain M of the converter is bigger than 1 when operating in Region 2.1. we use a transformer ratio equals to 4 to satisfy the requirement. Also, L_r and L_m are realized with discrete inductors.

The resonant capacitor has been used not only to eliminate the DC current, but also as a part of the resonant tank. Because the resonant energy is determined by the output power. We can obtain the information of C_r from the output voltage. Here an assumption is made to approximate the charging process of C_r. For $I_{cr} = I_o/N$, we can assume that in half of the switching period, C_r has been linearly charged from $-V_{crm}$ to $+V_{crm}$ (V_{crm} is the maximum voltage across C_r). Since the

charging time is half of the switching period, we can get:

$$\Delta V_{cr} = 2V_{crm} = \frac{I_o T_{s\max}}{2NC_r}$$

In this prototype converter, as long as the capacitor's value can meet the demand of safely operating, the capacitor can be selected. Thus, let's choose Cr = 470 nF, V_{crm} = 15.17 V. The ceramic capacitor we utilize has a voltage limit of +/- 25 V. Thus, the 470nF capacitor can operate safely.

Then:
$$Lr = \frac{1}{4\pi^2 f_r^2 Cr} = 8.43\mu H$$

The value of h is determined (h=Lm/Lr) by the switching frequency range. As discussed earlier,

$$V_o = \frac{V_{in}}{N} + \frac{(f_r - f_s)I_m}{4NCrf_s f_r} \qquad (4\text{-}1)$$

Based on circuit analysis, the voltage across Lm is NVo, and its charging time is half of the resonant period Tr/2 as discussed in Chapter 2. Thus, the current flow through Lm increases linearly. The maximum value of the resonant current can be derived as

$$I_m = \frac{NV_o T_r}{4L_m} \qquad (4\text{-}2)$$

Substituting (4-2) into (4-1), we can get:

$$V_o = \frac{V_{in}}{N} + \frac{\pi^2 V_o}{4h}\left(\frac{f_r}{f_s} - 1\right) \qquad (4\text{-}3)$$

As V_{in} = 40 V, we can substitute V_{in} into (4-3) and with the assumption that the Lm is large enough to maintain the resonant current value (I_{Lm} = I_{Lr}) in the second time interval at a fixed

value. we can get $\frac{f_{s\min}}{f_r} = \frac{\pi^2}{2h+\pi^2}$. In Dr. Bo Yang's dissertation [3], a conclusion was discovered that when h is relatively large, the converter has better performance but it degrades very fast as input voltage drops. When h is relatively small, the converter has more balanced performance for the whole range of input voltages, but the performance at high input voltage is greatly impaired. A common experience value range for h is between 3 to 7. Here, let's select h to be 6.76 and the L_m is set to be 55.4 μH.

As mentioned in Chapter 2, the loading resistance boundary between ZVS and ZCS is:

$$R_{lb} = \frac{\pi^2 h Z_r \omega_n}{8N^2} \sqrt{\frac{1-\omega_n^{\ 2}}{(1+h)\omega_n^{\ 2}-1}} \qquad (4\text{-}4)$$

Therefore, we substitute the transformer ratio N, resonant capacitor value C_r and the value of h into (4-4) and obtain R_{lbmax}=1.43 Ω, For R_{lmin}, 40/1=40 Ω. So, this converter will operate in ZVS switching mode over the full load range. The maximum ripple voltage on the output was set to be 10% of the rated output voltage and is 1V. It is complicated to determine the uncharged time for the filter capacitor because it's not only uncharged during stages 3 & 6 when there is no power flows to the secondary side, but also in other stages when the current flow through the filter is larger than I_o. Let's assume that the discharging time for C_f is T_s to make sure that the capacitor will surely satisfy the ripple requirement. Since the capacitor discharges at a constant value of I_o and the discharging time is set to be T_s, the value of C_f can be calculated as follows:

$$C_f = \frac{I_o T_{s\max}}{\Delta U_c} = \frac{1}{1*60*10^3} = 16.67\mu F \qquad (4\text{-}5)$$

Practically, we chose two parallel connected 10μF capacitors to reduce the ESR value for the

prototype circuit experiment.

4-2. Magnetics design

The transformer windings utilized Litz wire to reduce losses. We need to determine the number of strands for the Litz wire. The formula to calculate the skin depth is:

$$\delta = \frac{1}{\sqrt{\pi f \mu_0 \sigma}} \qquad (4\text{-}6)$$

Where σ is the conductivity of the conductor, f is the frequency of the current in the winding, and μ_0 is the permeability of free space [13]. In the circuit to be constructed, $\mu_0 = 4\pi*10^{-7}$ H/m, f = 80 kHz, and $\sigma = 5.8*10^7$ S/m (for copper wire). Thus, (4-6) can be written as

$$\delta = \frac{66.1}{\sqrt{f_s}} mm \qquad (4\text{-}7)$$

So, for $f_s = 80kHz$, we calculate the skin depth to be 0.23 mm.

Now we should find breadth b and turns per-section Ns. The concept of the breadth is shown in Fig 4.1. In Fig 4.1, "b" is the breadth of the winding across the face where one winding faces another. "Ns" is the number of turns in the section of the winding (In simple windings without interleaving, Ns=N). Each section shown has a number of turns *Ns* depending on whether the different sections of a given winding (primary P or secondary S) are in parallel or series. The total number of turns *N* for that winding may be equal to *Ns* or equal to product of *Ns* and the number of sections.

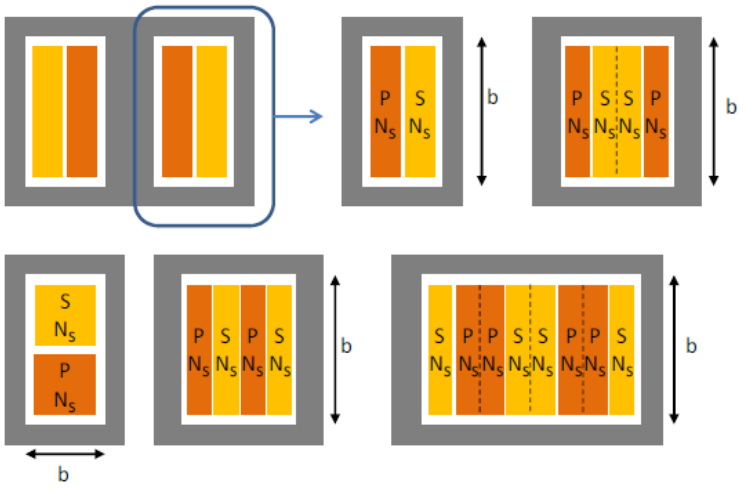

Fig 4.1 Examples of the winding breadth *b* and the number of turns per section [15]

Different strand AWG size and parameters are shown below:

Strand AWG size	32	33	34	35	36	37	38	39	40	41	42	43	44	45	46	47	48
Strand diameter (mm)	0.202	0.180	0.160	0.143	0.127	0.113	0.101	0.090	0.080	0.071	0.063	0.056	0.050	0.045	0.040	0.035	0.032
Economical F_R	1.06	1.07	1.09	1.11	1.13	1.15	1.18	1.22	1.25	1.30	1.35	1.41	1.47	1.54	1.60	1.64	1.68
k (mm^{-3})	130	203	318	496	771	1.2k	1.8k	2.8k	4.4k	6.7k	10k	16k	24k	36k	54k	79k	115k

Table 4.1 Parameters for Litz-wire selection[15]

The recommended number of strands for each of the strand diameters being considered is calculated [15]:

$$n_e = k\frac{\delta^2 b}{N_s} \qquad (4\text{-}8)$$

In (4-8), k can be found given in Table 4.1 in unit of mm^{-3}. So, b and δ should also be in units of mm. For coil 1: Ns = 11.21; δ = 0.21mm; b = 10.4mm; k = $130mm^3$. And n_e is determined to be 5.31. The skin depth has already been calculated and the wire we select should have smaller diameter. As a result, we picked #32 AWG wire and a strand number of 4 to approximately satisfy the recommended value of n_e. The recommended value of n_e should be taken as a general

guideline. Values of *n* as much as 25% above or below *ne* can still be good choices [15]).

Now let's check whether the designs given by (4-8) will fit in the window space available. To approximately determine the total area of actual copper, we can calculate the total area of the copper as *NnAs*, where *N* is the number of turns, *n* is the number of strands, and *As* is the cross sectional area of a single strand to estimate the area[14]. The product must be less than 25% to 30% of the window area to be available for the winding. Since we picked n = 4, As = 0.032mm^2, the number of turns for the two inductance (Lr and Lm) are Nlr = (L/Al)^0.5 = 11.21turns and Nlm = 24.88 turns. So the total area is 1.41 mm^2 for Lr and 3.2 mm^2 for $L_{m.}$ The magnetic core of the inductor was chosen as a Kool Mu toroid one, 0077324A7, produced by Magnetics. Inc. For the magnetic core 007324A7, A_L = 117 +/-8% nH/T^2. The window area is 364 mm^2 ,the cross section area Ae = 67.8 mm^2. Also, for the magnetic flux density during conduction is:

$$B = N * A_L * I / A_e = 12*117*10^{-9}*0.25/(67.8*10^{-6}) = 5.2*10^{-3}T$$

This magnetic flux density value can satisfy the commonly chosen criterion of the saturated value of 0.25 T. So, the magnetic core has been determined. Thus, the total winding area of the winding on the right half side of the core is 4.736 mm^2, which meets the maximum percentage of 25%.

For the design of the transformer, the magnetic ferrite core in the lab was used. Its type is an E41-3C90, which has an air gap of approximate 2.59 mm in length and the value of A_L to be 220 nH/turn. With the bobbin and Litz wire we have chosen, a transformer is made whose turn ratio is 4:1:1[16][17][18]. The transformer's diagram and its equivalent circuit is shown in Fig 4.2. In Fig 4.2, we should note that the transformer not only has a magnetic inductance that is parallel

connected to the primary side but also a leakage inductance that is series connected.

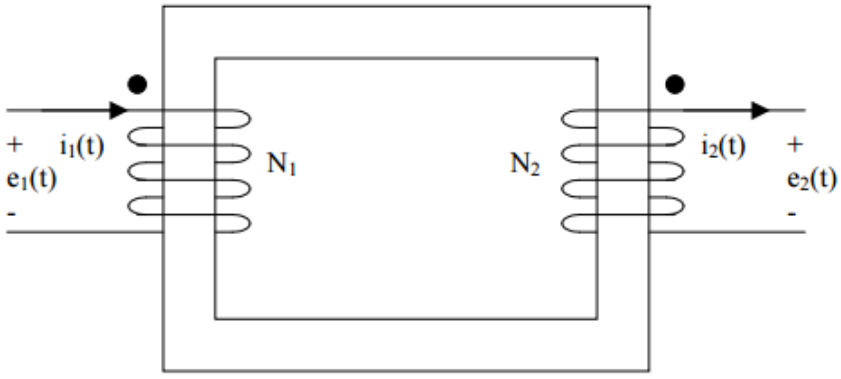

(a) Diagram for a transformer

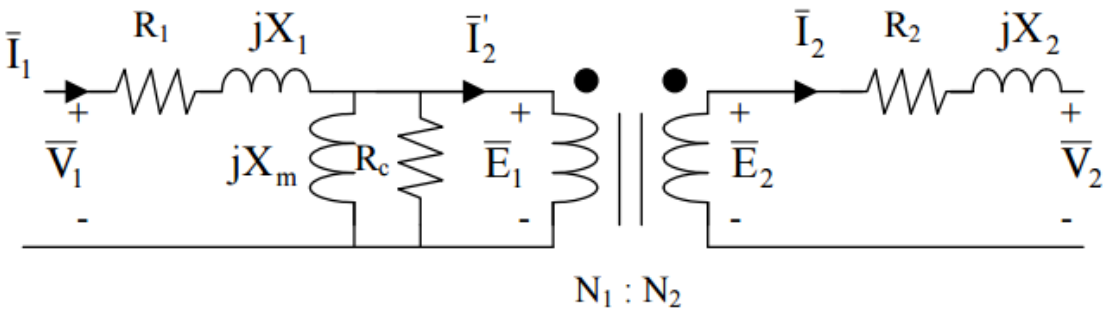

(b) Equivalent circuit for the transformer in Fig 4.2(a)

Fig 4.2 Diagrams of the transformer[19]

Therefore, the value of Lr is the sum of the inductance of the inductor we construct and the leakage inductance in the primary side of the transformer. In the lab, we utilized the frequency response analyzer to measure the values of L_r and L_m. The analyzer is the AP300 model from Ridley Engineering. The AP300 can measure the value of the inductance and its equivalent resistance as well.

Firstly, the magnetic inductance L_m is measured. The sweeping frequency range is selected to be 10 kHz to 100 kHz. The measurement result is shown in Fig 4.3. In the figure, we can directly see the measurement value of 52.3 μH.

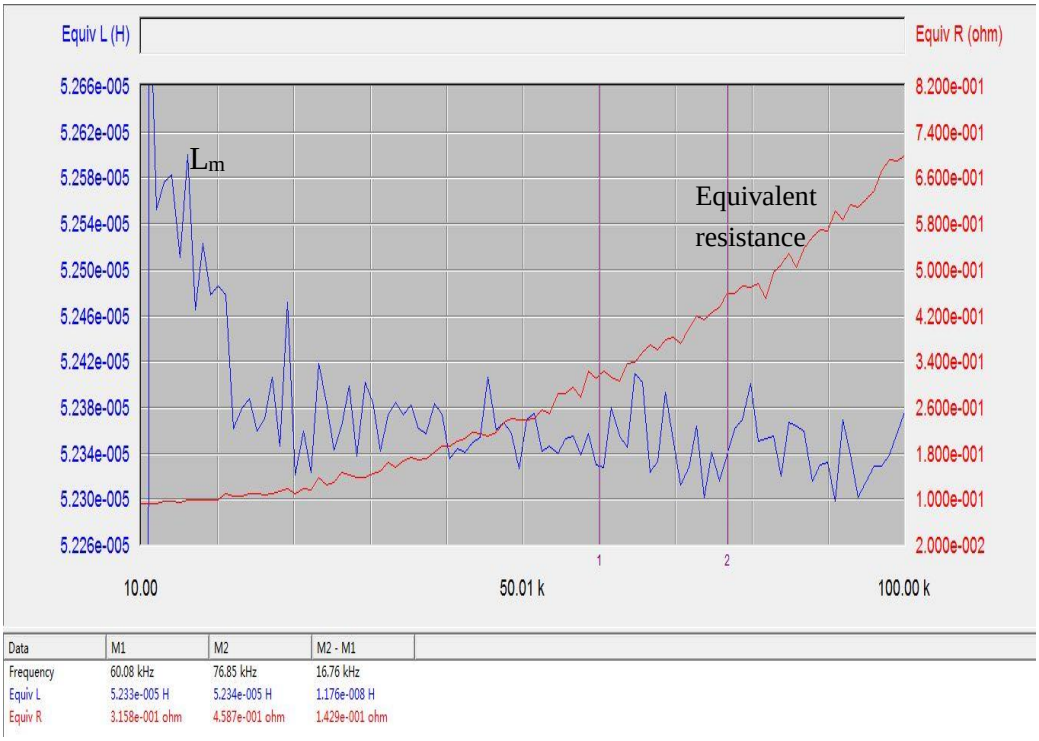

Figure 4.3. Magnetic inductance Lm=52.3 μH

Secondly, the leakage inductance of the primary side should be measured. To obtain this value, the secondary side is short circuited. The resulting measurement is shown in Fig 4.4.

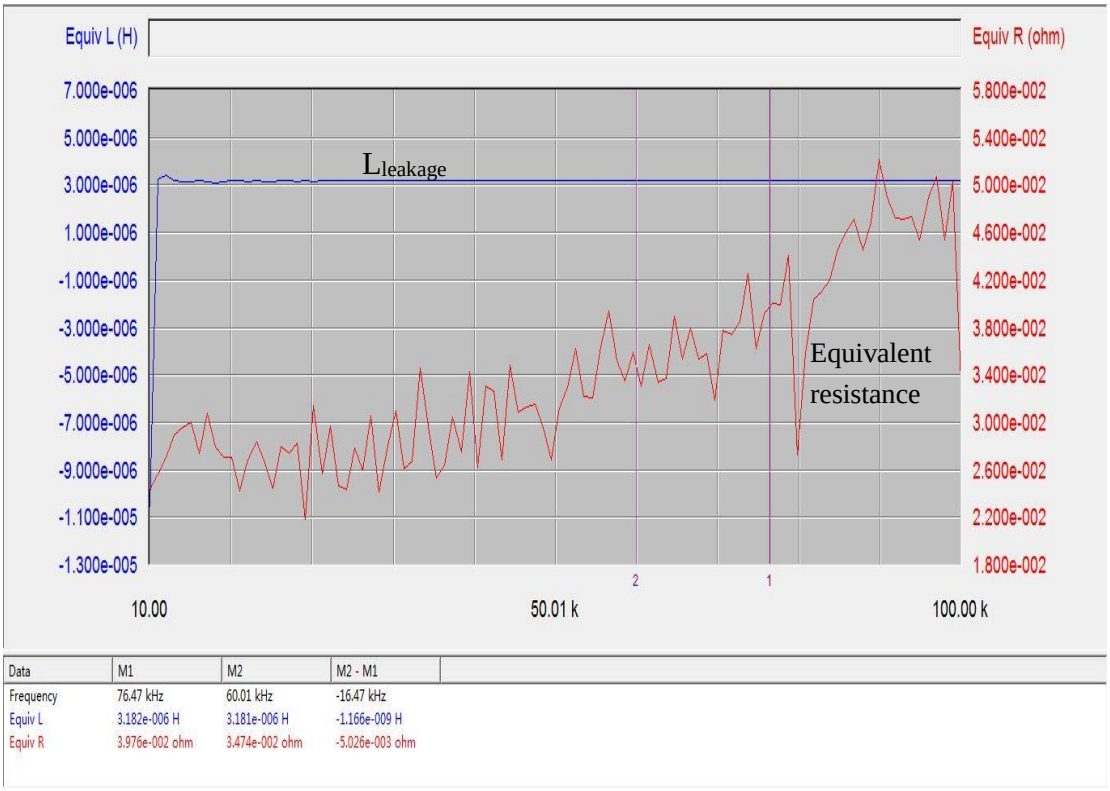

Figure 4.4. Leakage inductance Ll=3.18 µH

When inductors are connected in series, the equivalent inductance is the sum of each inductance when the resonant inductor Lr is constructed, we should make its value to be $L_{rpractical} = L_r - L_{leakage} = 8.43 - 3.18 = 5.25\mu H$. the practical value of $L_{rpractical}$ may have some deviation from the ideal value. The measurement result is shown in Fig 4.5.

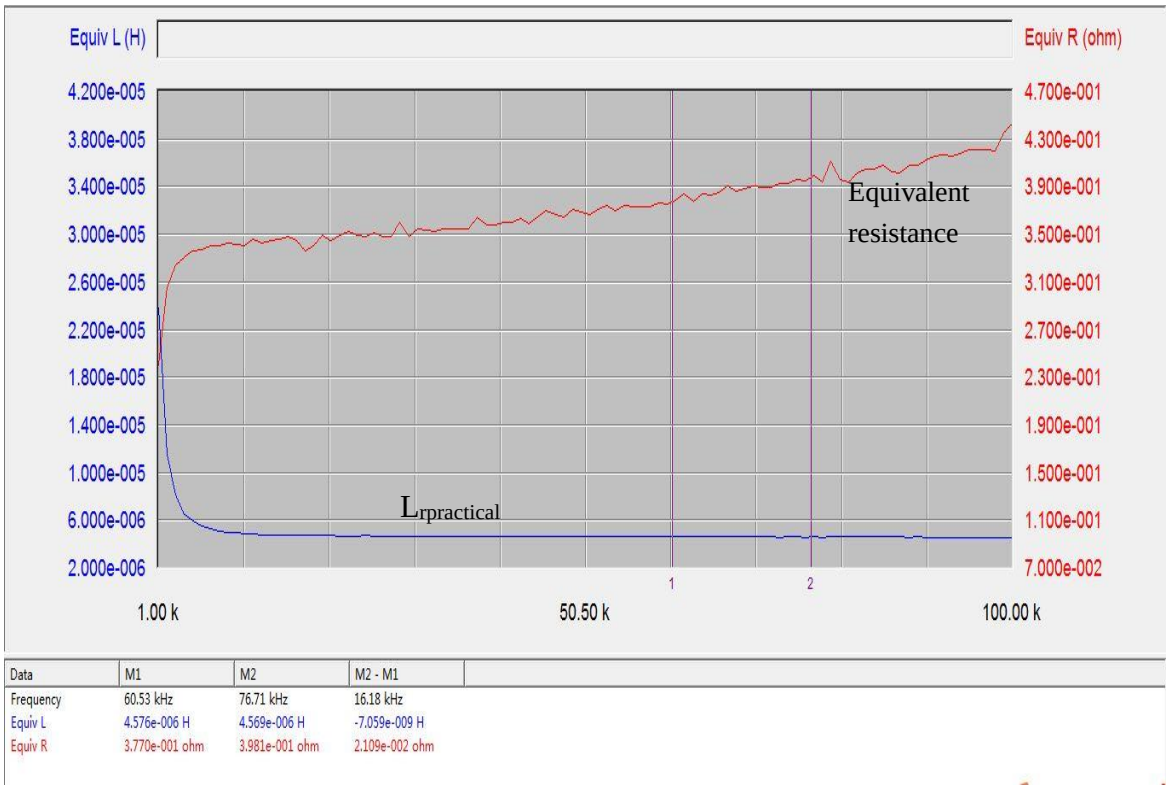

Figure 4.5 Resonant inductance Lr=4.57μH

In the meantime, not only the primary side has leakage inductance, the secondary side also has leakage inductance. Since the transformer is center-tapped, there should be two leakage inductance paralleled connected in the circuit. The secondary leakage inductance may not be a part of consideration during building the transformer, but we should also measure them to optimize the simulation results. The measurement results are shown in Fig 4.6.

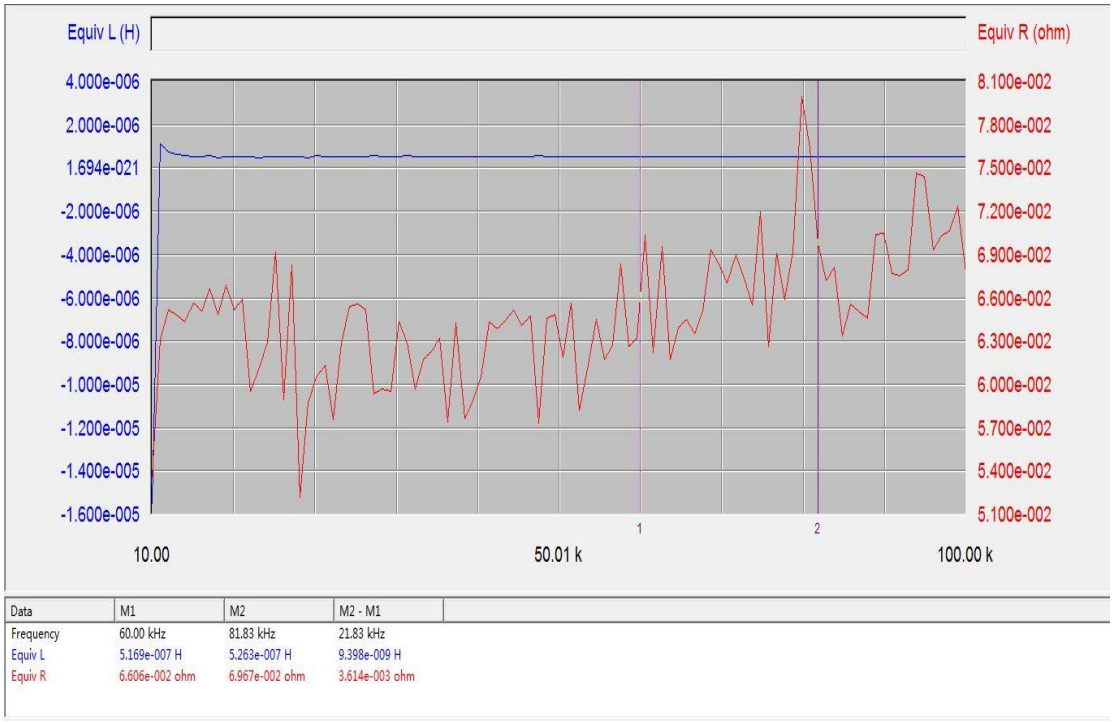

Figure 4.6 (a). Leakage inductance of the secondary side 1

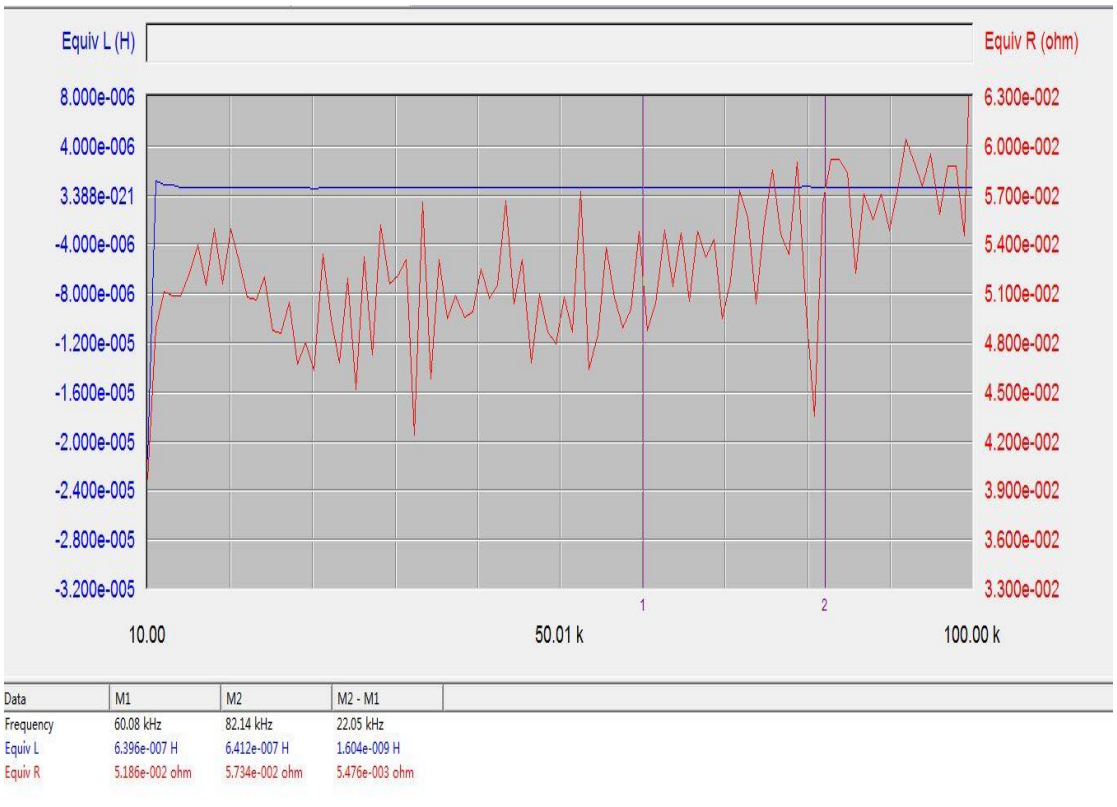

Figure 4.6 (b). Leakage inductance of the secondary side 2

Also, since the resonant capacitor and the filter capacitor have already been selected. The multi-layer ceramic capacitors produced by Mallory Inc. were simply chosen at the desired value. Finally, for the load, two fixed value resistors and a variable resistor were picked. The two fixed value resistors have resistance of 10 Ω and 25 Ω. The variable resistor's resistance is 3 Ω. The 3 Ω and 10 Ω are series connected, and the 25 Ω one is parallel connected to them.

4-3. Circuit driving and analog control circuit

When the circuit operates properly, the upper MOSFETs in the bridge circuit are floating. In order to achieve the floating drive of the switches, driving chips are utilized in this circuit to drive these MOSFETs. With a commonly used analog chip IR 2110, the voltage between the gate and source can be 10V [20]. As a result, the switches can operate simultaneously with the feedback signal from the control chip's output. Thus, the circuit diagram can be redrawn as shown in Fig 4.7.

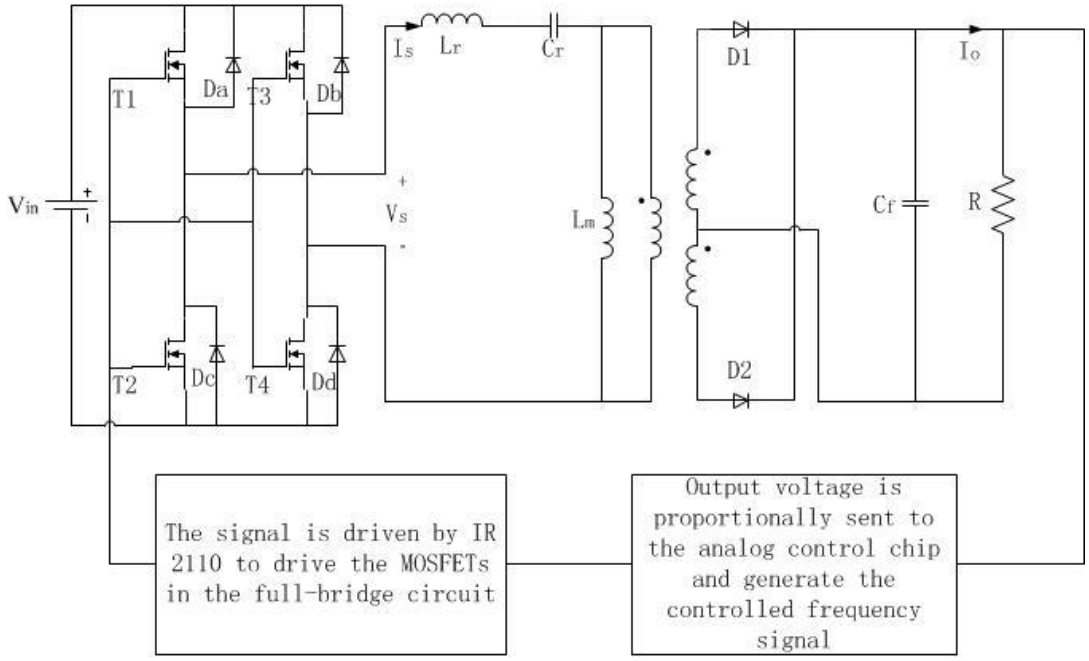

Fig 4.7 Circuit diagram of the prototype LLC resonant converter

The circuit operating diagram is shown in Fig 4.8

Fig 4.8 Control block diagram

Also, the Miller Effect should be considered. When operating at such high frequency, the capacitance formed between the gate and drain of MOSFET will affect their operation. To eliminate the Miller Effect, an additional emitter capacitor is used to shunt the Miller current. Due to this additional capacitor, the required drive power is increased [21]. The method used to reduce the Miller Effect is shown in Fig 4.9.

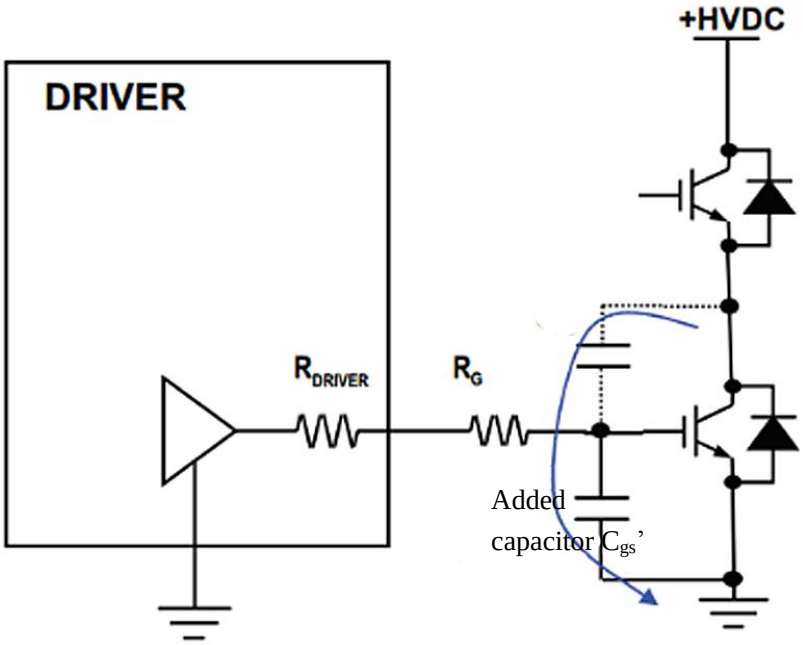

Fig 4.9 Additional capacitor between gate and source [21]

The analog control chip MC34066 (high performance resonant mode controller) is utilized to regulate the converter's output voltage. It can be utilized to modulate the switching frequency through modulated constant on-time or constant off-time control[20]. The upper limit of the

frequency can reach 1MHz. The MC34066's core components are a reference voltage generator, a variable frequency oscillator, an error amplifier, a soft-start circuit and a output circuit. The inner structure of the chip is shown in Fig 4.10.

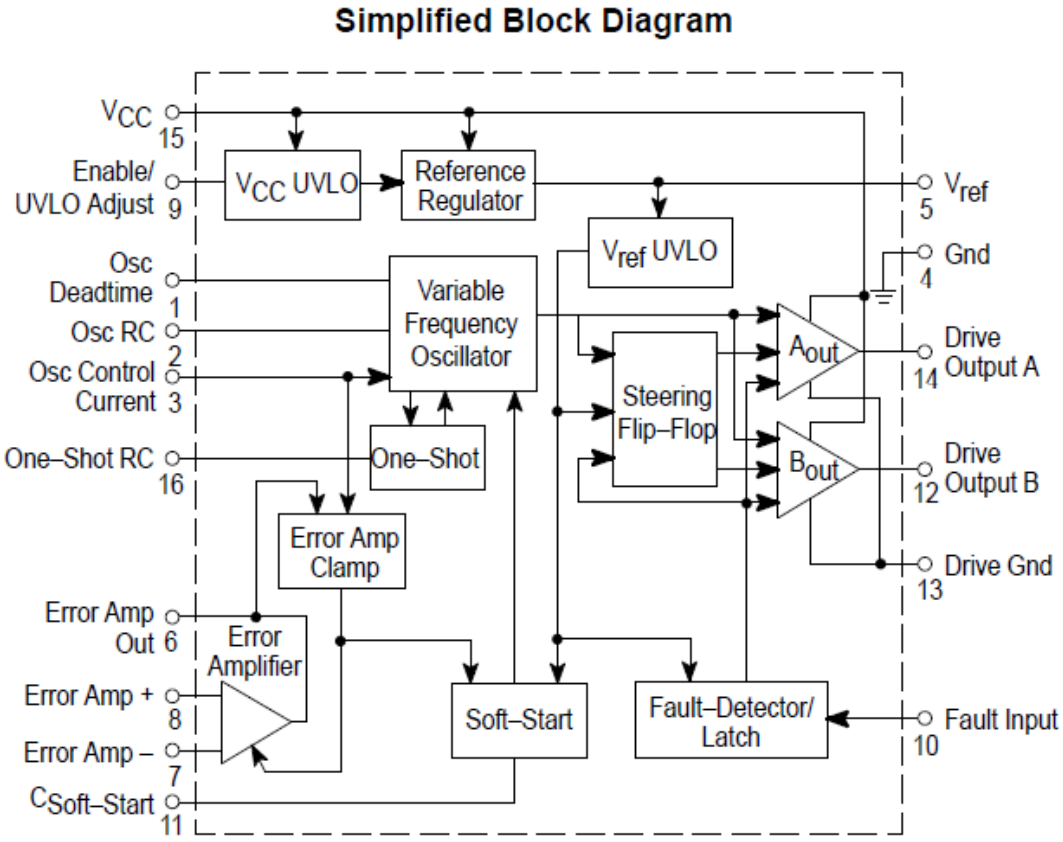

Fig 4.10 Inner structure of the MC34066 [22]

4-3-1 Reference voltage source

This part of the chip can provide a reference voltage of 5.1 V, and can provide 10 mA of current to the output as well.

4-3-2 Variable frequency oscillator

The output signals are produced by the oscillator. The circuit contains two double-threshold comparators, a constant current source and an RC charge-discharge circuit. As

seen in Fig. 4.11, when capacitors Cosc and C_T are charged, a maximum voltage of 5.1 V is generated across the two capacitors. The output signal will change states at 3.6 V. Also, the dead time is determined by the value of R_{DT}, at a range of 0 ns to 800 ns as R_{DT} varies between 0 Ω and 1 kΩ.

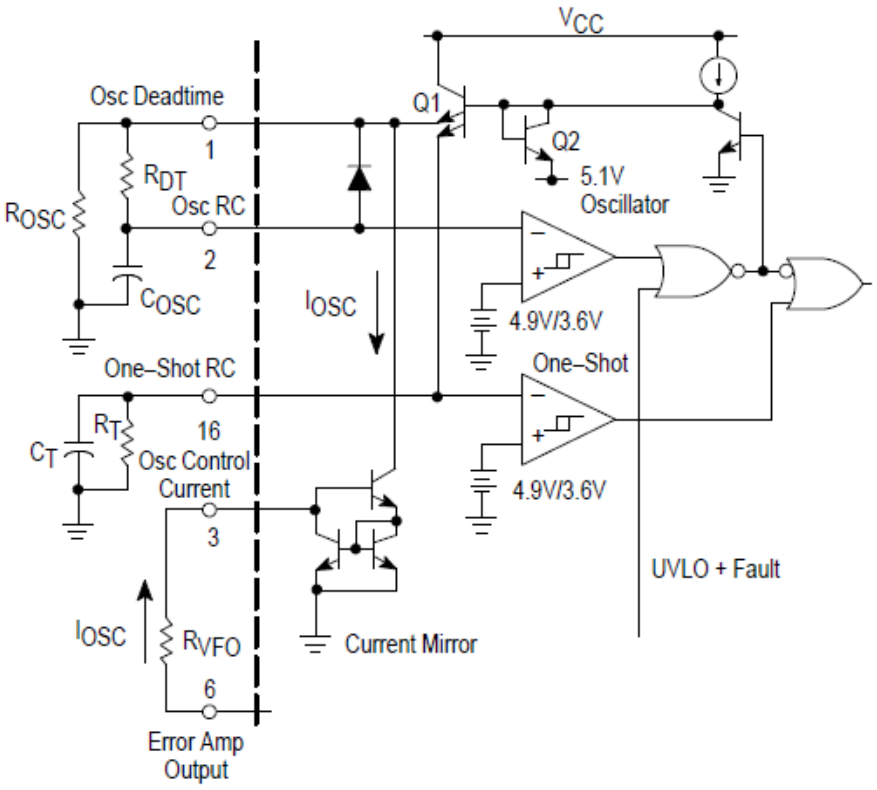

Fig 4.11 Oscillator and one-shot timer [22]

By choosing the oscillator discharge time (t_{dchg}) value and the one shot time, the user can freely choose the operating mode of the oscillator. Two different modes are shown in Fig 4.8. In Fig 4.8, when t_{dchg} is bigger than $t_{one\text{-}shot}$, the turn on time in each period is fixed and the turn off time varies. On the contrary, when t_{dchg} is smaller, the duty cycle is changed due to the variation of t_{dchg}.

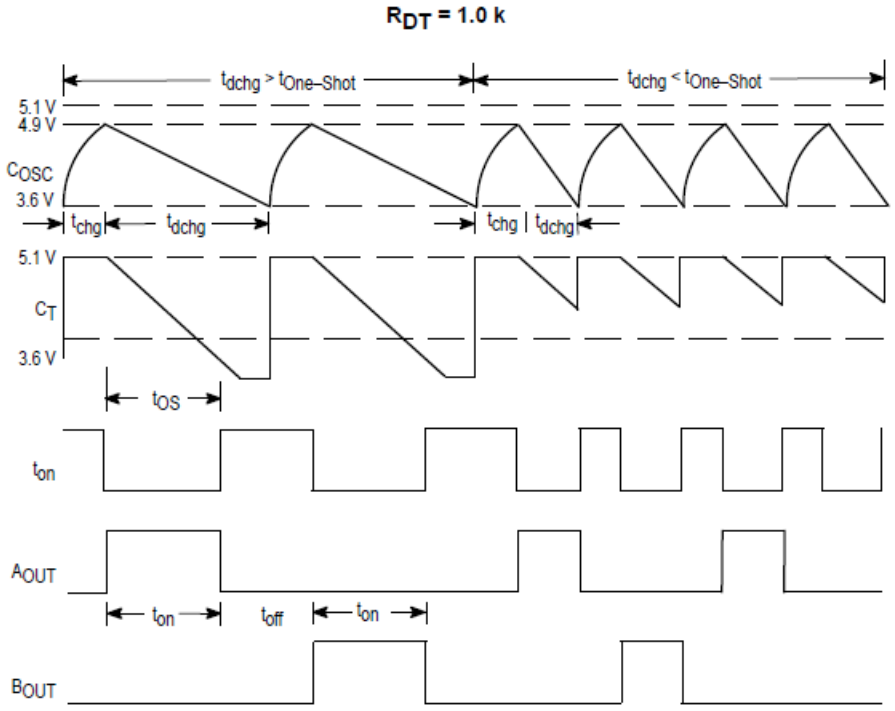

Fig 4.12 Timing waveform at 800ns dead time[22]

Capacitors and resistors values used in the circuit are shown in Table 4.2.

C_{osc}	R_{osc}	R_{VFO}	R_{DT}	C_T	R_T
330pF	68kΩ	100kΩ	1kΩ	22nF	680Ω

Table 4.2 Capacitors and resistors used with the MC 34066

As we've already discussed, the method to control the output voltage of the converter is to change its operating frequency. Thus, PWM is not suitable for control since the frequency of the PWM waveform is a fixed value. The LLC resonant converter designed operates in pulse frequency modulation (PFM) mode [23]. Therefore, we should let the chip operates in the mode of $t_{dchg} > t_{One-Shot}$. Pins 7, 8 are input ports of the amplifier. Because the LLC converter operates in

Region 2.1, we connect pin 7 to the reference voltage of 5.1 V and connect the feedback voltage signal to pin 8 to realize negative feedback to the prototype circuit. As a result, the output frequency signal can be sent to the driving circuit and utilized to adjust the switching frequency of the converter. The driving and analog control circuits are shown in Fig 4.13.

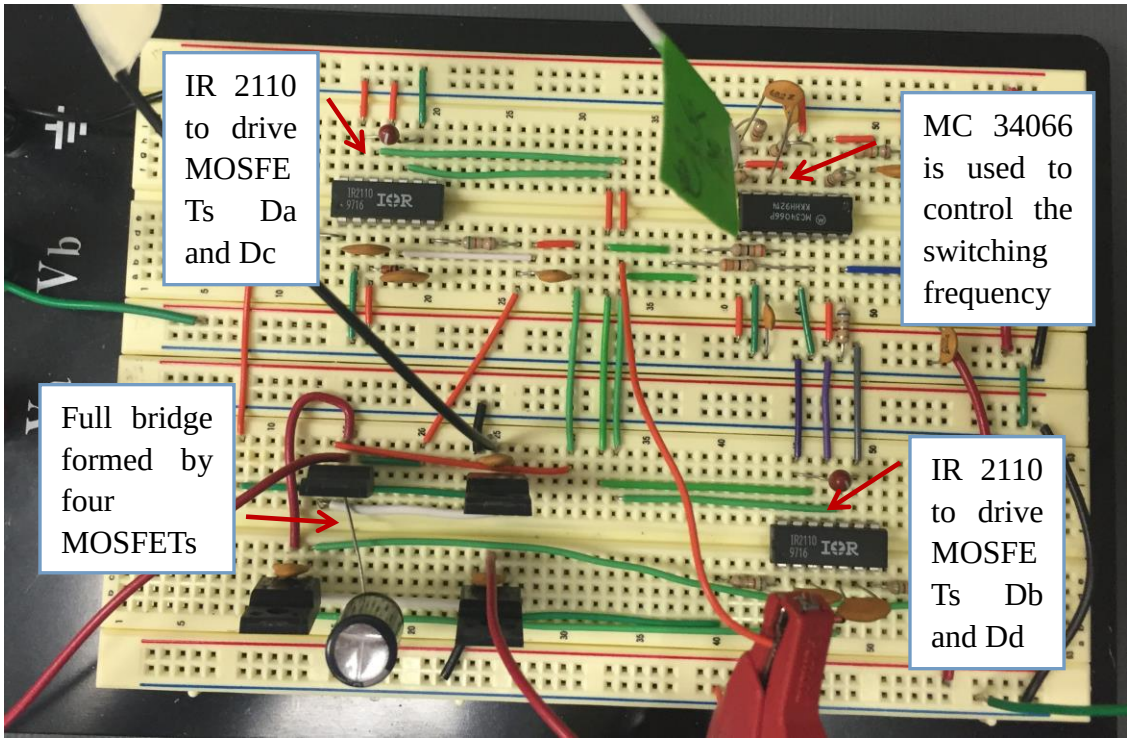

Fig 4.13 Driving and analog control circuit of the prototype converter

In this chapter, the parameters used for the prototype LLC resonant converter are selected at first. Then the detailed process of designing magnetic components was illustrated. After the main circuit of the converter was constructed. The periphery circuits were designed. The driving circuit formed by the IR 2110 was designed and the Miller effect was reduced. Then the analog control chip MC 34066 was introduced and its periphery circuit was designed. As a result, the construction of the hardware circuit was completed. In the next chapter, experimental results will be shown.

CHAPTER 5. Simulation and experimental results

In order to verify the correctness of the theory proposed in the former chapters, simulation results are presented in this chapter. Meanwhile, a prototype of the LLC resonant converter was constructed and tested. The parameters of the converter were selected in Chapter 4. Recall that the converter parameters are:

$$V_{in}: 36 \sim 40V;\ f: 60kHz \sim 80kHz; V_o \approx 10.7V;$$
$$C_r = 470nF; L_r = 7.76\mu H; L_m = 52.5\mu H; C_f = 20\mu F$$

5-1. Analysis of simulation results

The software SIMPLIS has been used to simulate the operation of the prototype LLC resonant converter constructed, Fig 5.1 is the simulation schematic. As mentioned earlier, the practical transformer doesn't only have leakage inductance on the primary side, but also on the secondary side. Therefore, leakage inductance values were included in Fig 5.1.

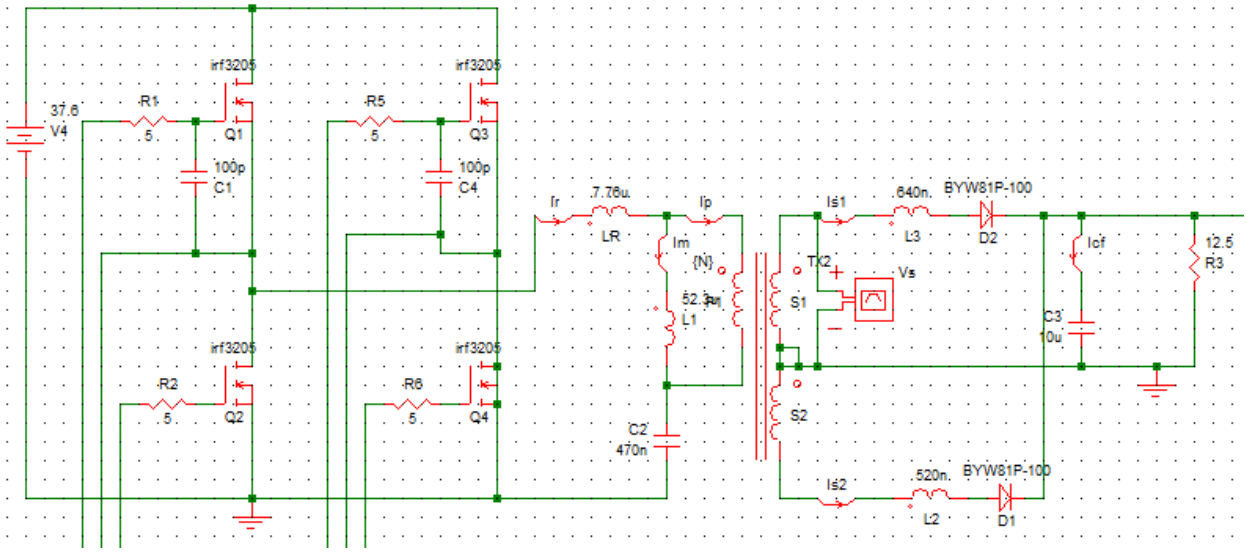

Fig 5.1 Simulation diagram for the LLC resonant converter in SIMPLIS

The simulation result is shown in Fig 5.2. Presented in Fig 5.2 (a) is the resonant current

waveform. In the simulation result, we can clearly see the current flowing through L_m increases linearly until reaching I_m. Then the converter moves into the second time interval, and L_m participates in the resonance. In Fig 5.2 (b), the output voltage is 10.7 V which is the same as the experimental result. Here we should notice that because the voltage transforming ratio of the practical transformer is not the idealized ratio, the output voltage of the simulation and experiment may not be exactly equal to each other.

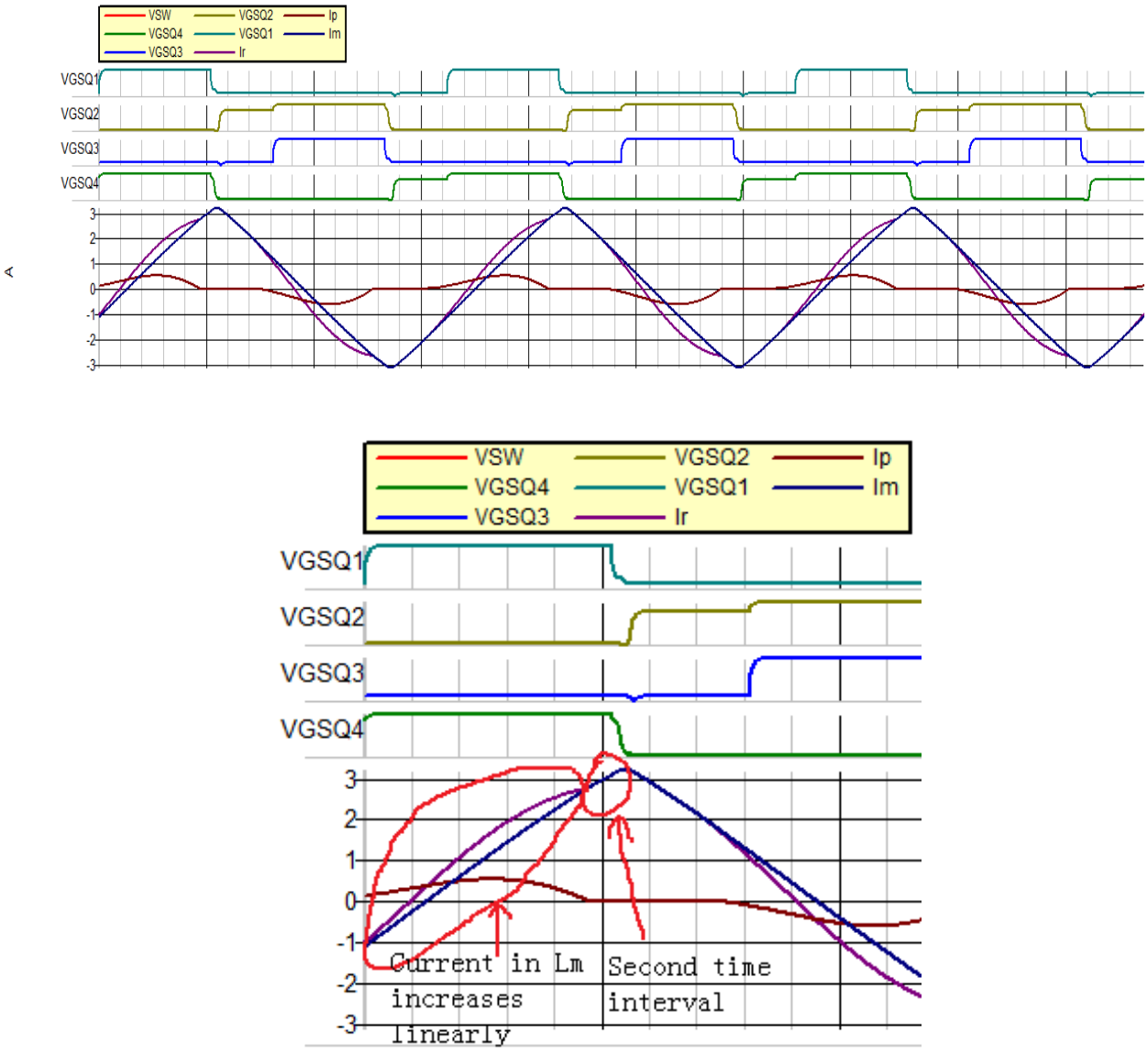

Fig 5.2 (a). Resonant current during converter operation

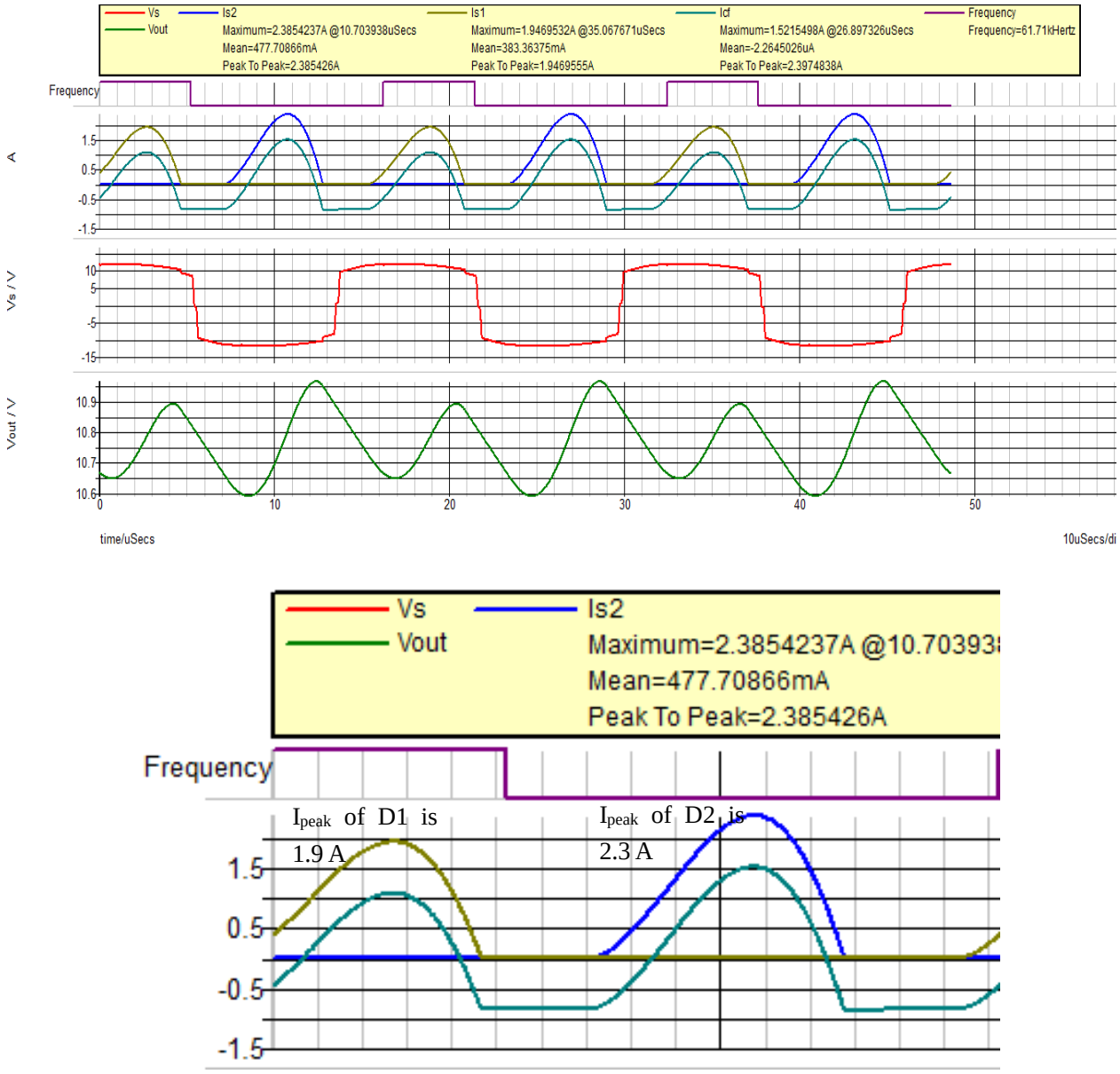

Fig 5.2 (b). Current in the secondary side of the transformer and the output voltage

Due to the simulation result, the operation of the converter can be verified. Also, we've considered the effect of the leakage inductance of the primary side and made it as a part of the resonant inductor L_r. Also, the secondary side of the transformer has leakage inductance. When simulating the converter, two different value of inductors were added to the secondary side to make the simulation result more practical. That's the reason why the current flowing through the

diodes D1 and D2 are not exactly the same. The result is shown in Fig 5.2 (b).

5-2. Experimental results

An experimental converter was constructed including the analog control circuitry and the hardware circuit as shown in Fig 5.3. Because the external resistors and capacitors connected to the analog control chip MC 34066 are not precisely equal to the calculated values, the output frequency may have a slight deviation compared to the expected value. The practical operating frequency range was 60 kHz to 79 kHz, which does not perfectly matching the design range.

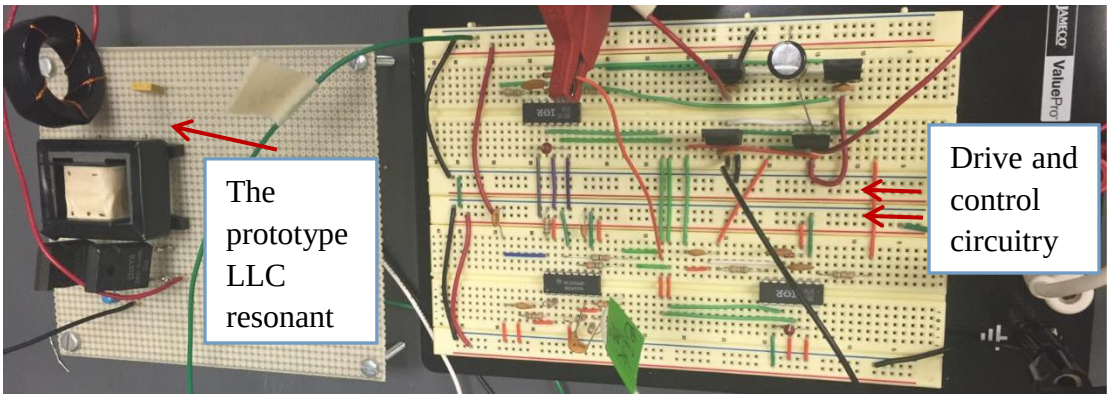

Fig 5.3 Prototype of the LLC resonant converter

After powering on the circuit, it operated at the desired frequency at 79 kHz. Using DC coupling on the oscilloscope, a perturbation was added to the load. As mentioned earlier, the load was formed by parallel connected resistors. To realize the perturbation, the parallel connected 25 Ω resistor was disconnected. The dynamic response was captured when the disconnection occurs. In the experiment result, a slight variation in the output voltage is shown in Fig 5.4. The output voltage returned to 10.7 V.

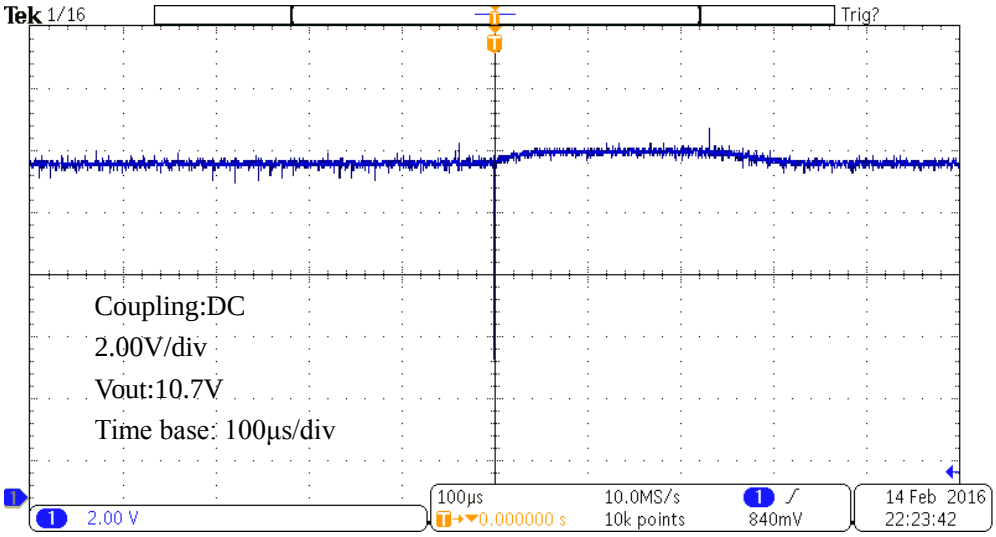

Fig 5.4. Output voltage test for the converter

Fig 5.5 shows the resonant current flow in the resonant tank when the converter was operating. It clearly shows two time intervals as in Fig 5.2 (a).

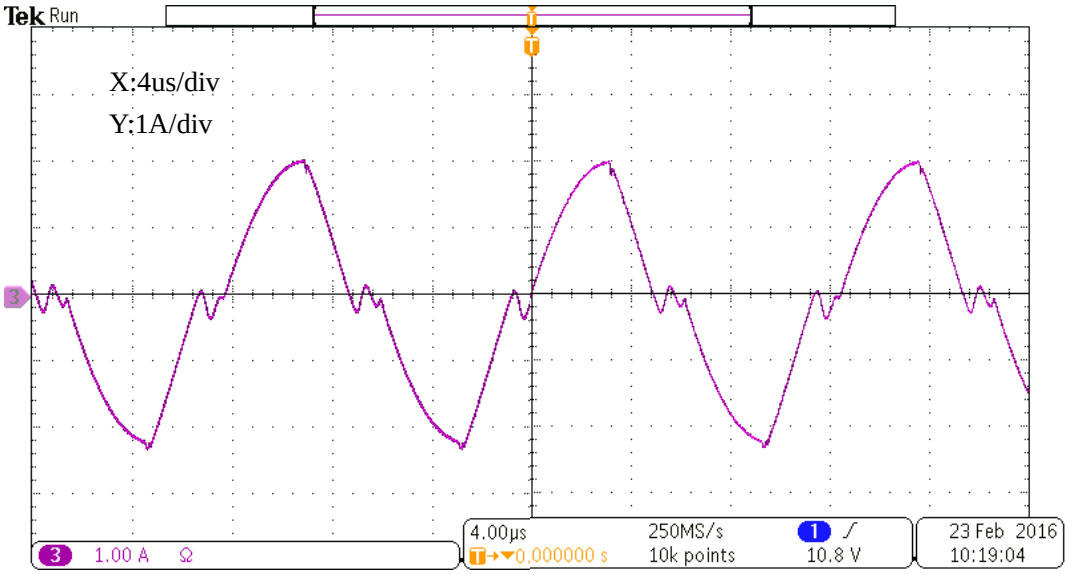

Fig 5.5 Current flows in resonant tank

Because the ratio of the transformer was 4 and the load and input voltage variation range was limited, more data is needed to verify the success of the control method. Therefore, several test results were recorded. Since there are two perturbations (load and input voltage), tests were

made in two groups. One was changing the load with a fixed input voltage, and another one was changing the input voltage with a fixed load. The input power can be simply calculated by V_{in}*I_{in}. The output power is calculated by $I_o^2 * R_L$. Thus the converter's efficiency is (P_o/P_{in})*100%. Also, another channel is connected to the frequency signal at the output of MC34066. The ocsilliscope used was a Tektronix MDO3000, which can automatically measure the operating frequency during operation.

Table 5.1 shows different output voltages and power efficiency at a certain input voltage value of 36 V.

Output power(W)	Switching frequency(kHz)	Input current(A)	Efficiency
9.16	77.4	0.31	82.08%
10.41	71.8	0.36	80.32%
11.45	68.2	0.40	79.51%
12.48	66.8	0.44	78.78%
14.05	64.9	0.49	79.65%

Table 5.1 Constant input voltage and varying loads

Table 5.2 shows efficiency variations when input voltage was varied and the load was fixed at 10 Ω. While, the output voltage was fixed at 10.7 V. Thus, the output power was 11.45 W.

Input voltage(V)	Switching frequency(kHz)	Input current(A)	efficiency
38.6	78.3	0.34	87.25%
38	69.1	0.36	83.70%
37.5	67	0.38	80.35%
36	64.7	0.40	79.51%

Table 5.2 Constant load and varying input voltages

Steady state tests were captured and recorded by the oscilloscope. Figure 5.6 to Fig 5.9 show the performance of the prototype circuit when either a perturbation occurs in the output load or input voltage. As mentioned earlier, the perturbation of the output load can be realized by connecting or disconnecting the parallel connected resistor. The input voltage perturbation is realized by adjusting the output voltage of the DC voltage source used in lab.

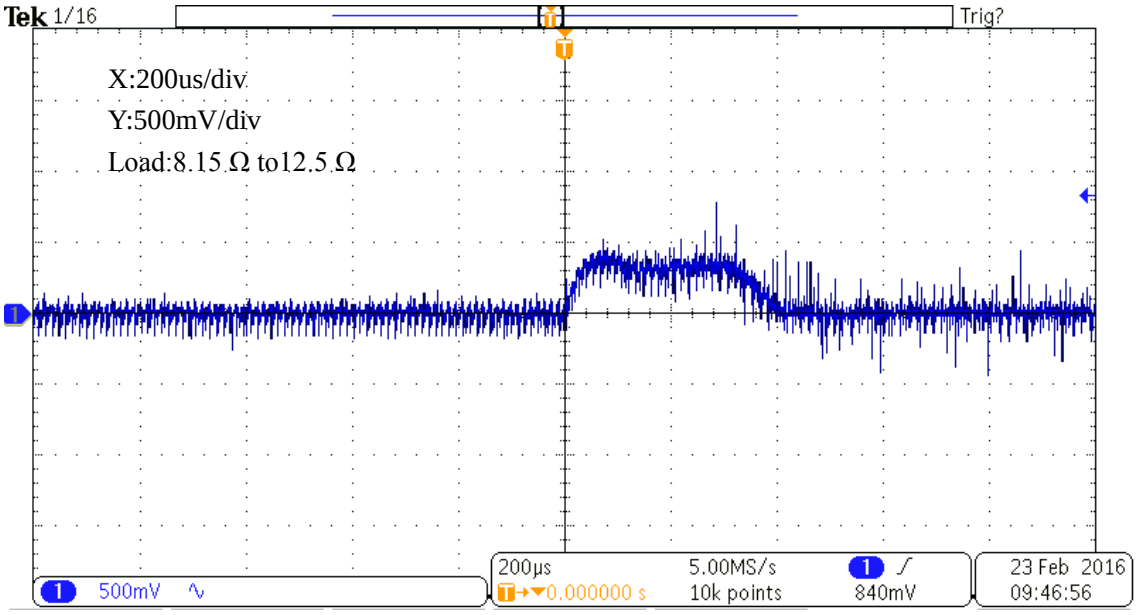

Fig 5.6 Load change from 8.15 Ω to 12.5 Ω

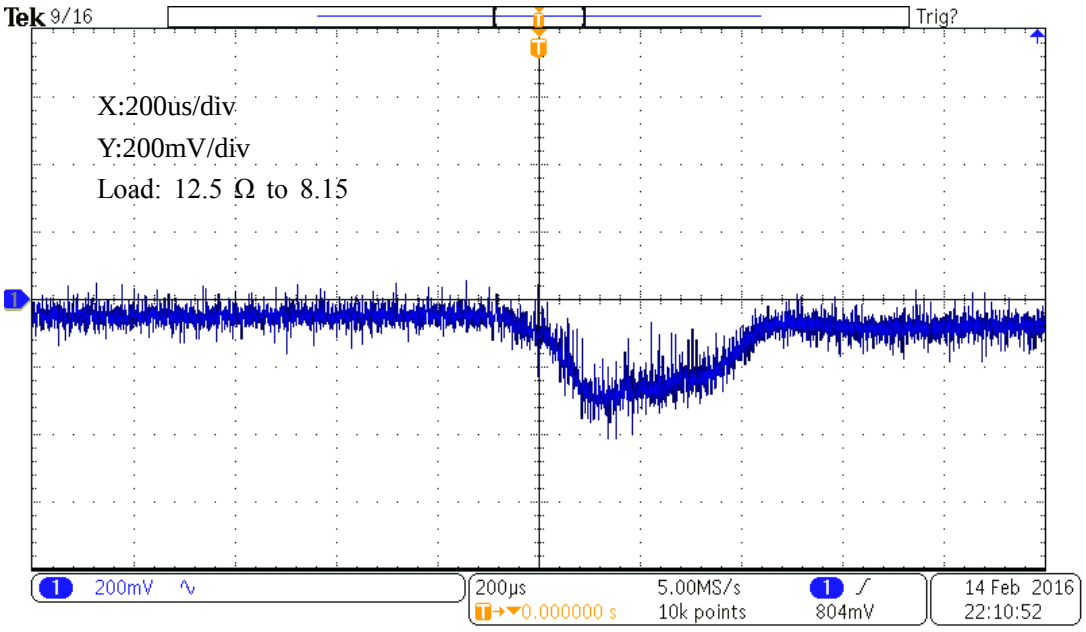

Fig 5.7 Load changes from 12.5 Ω to 8.15 Ω

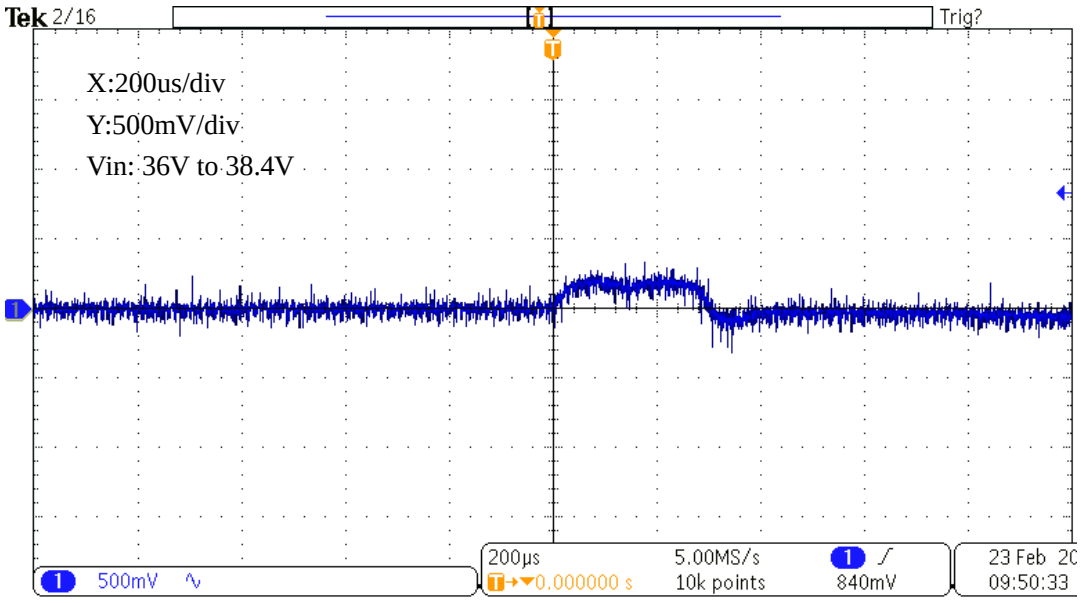

Fig 5.8 Input voltage change from 36 V to 38.4 V

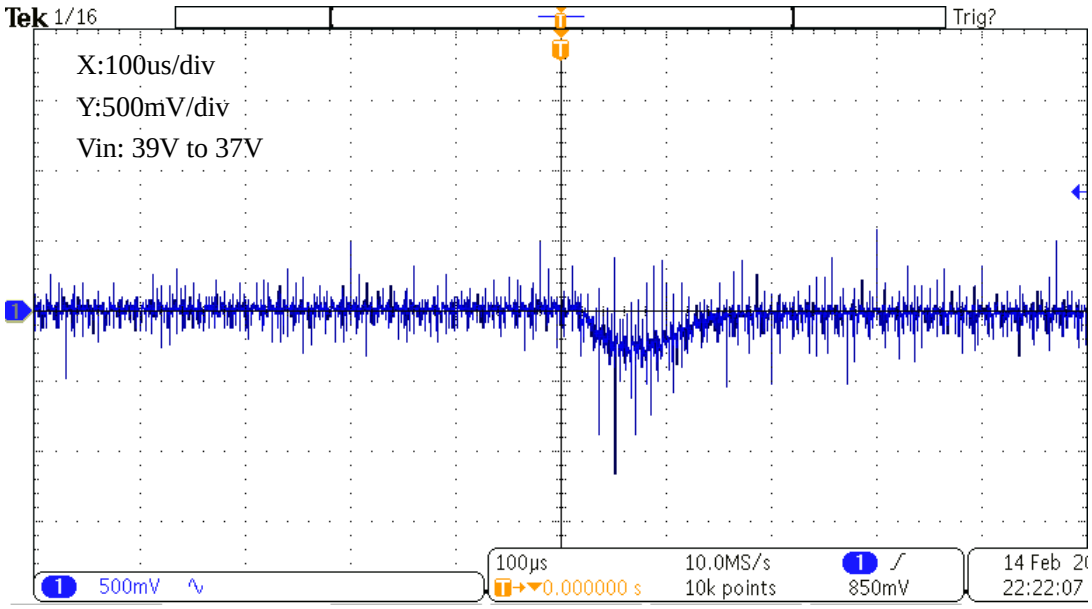

Fig 5.9 Input voltage change from 39 V to 37 V

Fig 5.6 to Fig 5.9 shows the result of the steady-state tests of the converter for changes in the input voltage and load. In these figures, the AC coupling mode was utilized, and the transient was captured. From these figures, the DC characteristic of the LLC resonant converter can be verified, along with the PFM control strategy. The output voltage remained fixed at 10.7 V when perturbations occurred in both the input voltage and load. As a result, the prototype of the LLC resonant converter has the ability to maintain the steady state output voltage.

CHAPTER 6. Conclusions

Nowadays, LLC resonant converters are utilized in many kinds of occasions, such as a Data-center, photovoltaic devices and also most commonly seen household appliances like LED TV sets and microwave-ovens. With more controlling methods proposed and applied, along with more periphery techniques utilized to optimize the resonant converter, the LLC resonant converter would be a crucial kind of power electronics technique that contribute to the human society.

In this thesis, the LLC resonant converter has been discussed in several aspects. Firstly, its DC characteristics were presented and its operation was described. Then the small signal model was presented through the method of extended describing functions. In addition, a control method has been proposed. After theoretical analysis, a prototype converter was constructed.

The analysis and operating region were verified using simulation. The operation of the converter was verified experimentally. The output voltage remained fixed for changes in the input voltage and load. In addition, the output ripple was reduced to a satisfied level due to the selection of the appropriate filter capacitor.

The experimental results may vary a little from the simulation result. However, the converter circuit obtained the goal of maintaining its output voltage to a certain value when there are perturbations in both the load and the input voltage.

Also, there are still some future work and suggestions. Firstly, integrated magnetics can be applied to the circuit [24]. The circuit volume can be significantly reduced with the integrated magnetic technique utilized. Also, circuit isolation should also be considered. In order to achieve

the isolation between the control circuit and the main circuit, a high-speed optocoupler or isolation transformer can be applied to the circuit. Thirdly, the usage of LLC resonant converters is not limited to household appliance but also power grid devices as well. Therefore, more experiments in high-voltage mode should be tested in order to get a more precise conclusion on its efficiency.

BIBLIOGRAPHY

[1] Erickson, Robert W., Dragan Maksimovic, Fundamentals Of Power Electronics. Springer Science & Business Media, 2001

[2] Bob Mammano, Resonant Mode Converter Topologies, Texas Instrument Technical Documents, 2001

[3] Bo Yang, “Topology Investigation for Front End DC/DC Power Conversion for Distributed Power System.” Ph.D. dissertation, Virginia Polytechnic Institute and State University, 2003.

[4] Vrej Barkhordarian, “Power MOSFET Basics”, International Rectifier Technical document, El Segundo, CA, Available: www.irf.com/technicalinfo/appnotes/mosfet.pdf.

[5] Arendt Wintrich, Ulrich Nicolar, Werner Turskey, Tobias Reimann. “Power Semiconductors Application Manual”, SEMIKRON International GmbH, Nov 2010.

[6] Lazar, J.F., Martinelli, R., "Steady-state analysis of the LLC series resonant converter," in Applied Power Electronics Conference and Exposition, pp.728-735, vol.2 2001.

[7] Yang, B., Lee, F.C., Zhang, A.J., Guisong Huang, "LLC resonant converter for front end DC/DC conversion," in Applied Power Electronics Conference and Exposition (APEC), 2002, pp.1108-1112 , vol.2, 2002.

[8] H. Ma, Q. Liu and J. Guo, "A sliding-mode control scheme for llc resonant DC/DC

converter with fast transient response," IECON 2012 - 38th Annual Conference on IEEE Industrial Electronics Society, Montreal, QC, pp. 162-167, 2012.

[9] Yu Fang, Dehong Xu, Zhang Yanjun, Fengchuan Gao, Lihong Zhu, Yi Chen, "Standby Mode Control Circuit Design of LLC Resonant Converter," in Power Electronics Specialists Conference, 2007. IEEE, pp.726-730, 17-21 June 2007.

[10] Eric X. Yang. “Extended Describing Function Method for Small-Signal Modeling of Resonant and Multi-Resonant Converters.” Ph.D. Dissertation, Virginia Polytechnic Institute and State University, 1994.

[11] Groves, J., "Small-signal analysis using harmonic balance methods," in Power Electronics Specialists Conference, pp.74-79, 24-27 Jun 1991.

[12] Yang, E.X., Lee, F.C., Jovanovic, M.M., "Small-signal modeling of LCC resonant converter," in Power Electronics Specialists Conference, pp.941-948 vol.2, 29 Jun-3 Jul 1992.

[13] Clayton R. Paul. Electromagnetic Compatibility, 2nd Edition John Wiley & Sons Inc. 2006.

[14] Sullivan, C.R., "Optimal choice for number of strands in a litz-wire transformer winding," IEEE Transactions on Power Electronics, vol.14, no.2, pp.283-291, Mar 1999.

[15] Sullivan, C.R., Zhang, R.Y., "Simplified design method for litz wire," in Applied Power

Electronics Conference and Exposition (APEC), pp.2667-2674, 16-20 March 2014.

[16] Ferroxcube Inc. Magnetic core E411712 Data Sheet. Sep 2008.

[17] AP Instruments Inc.Model 300 0.01 Hz - 30 MHz Frequency Response Analyzer users' manual, 2007.

[18] Colonel Wm. T. McLyman, Transformer and Inductor Design Handbook, 4th edition, Marcel Dekker Inc. 2004.

[19] Mark Halpin, Auburn Univeristy ELEC 5630/6630/6636 Course Note of Electric Machines, Spring Semester 2015.

[20] Infineon Inc, High and low side driver IR2110 data sheet, 2005.

[21] "Mitigation methods for parasitic turn on effect due to miller capacitor" Avago Technical Note AV02-0599EN, 2007.

[22] Motolora Inc. Motorola Analog IC Device Data MC34066, 1999.

[23] Zhengmao Zhang, Zhide Tang, "Pulse frequency modulation LLC series resonant X-ray power supply," in Consumer Electronics, Communications and Networks (CECNet), pp.1532-1535, 16-18 April 2011.

[24] Yang, B., Chen, R., Lee, F.C., "Integrated magnetic for LLC resonant converter," in Applied Power Electronics Conference and Exposition (APEC), pp.346-351 vol.1, 2002

APPENDIX. COMPUTER PROGRAM FOR SMALL SIGNAL MODELING

The computer program is utilized to calculate the small signal model of the LLC resonant converter. The whole computer program is shown in Dr. Eric Yang's dissertation [10] appendix. However, the computer program shows the process of calculating SRC resonant converters. The file "topo.m" should be modified to the LLC resonant converter we've designed.

The computer program for defining the LLC resonant converter is shown below:

```
%%%%%%%%%%%%%%%%%%%%%%%%%%%%%%%%%%%%%%%%%%%%%%%%%%%%%

% Name: topo.m -------- LLC topology
% Function: define converter circuit, operating condition,
% and switching boundary condition
% x ------------- current state vector
% u ------------- current input vector
% cur_mode ------ current topological mode
% t ------------- current time
% Output: num_mode ------ # of modes in one cycle
% Para ---------- Circuit Parameters
% x0 ------------ initial condition
% U0 ------------ given input vector
% CTL ----------- Control Parameters
% harm_tbl ------ harmonic table (see Chap.3)
% switching ----- 1 = not cross switching boundary
% -1 = cross switching boundary
% A, B, C, D ---- state matrices of current mode
% Ab,Bb,Cb,Db---- boundary matrices of current mode
%
% Calling: none
%
%%%%%%%%%%%%%%%%%%%%%%%%%%%%%%%%%%%%%%%%%%%%%%%%%%%%%
function [switching, num_mode, dim_out, harm_tbl, x0, U0, Ts, ...
   A, B, C, D, Ab, Bb, Cb, Db] = topo(cur_mode, x, u, t)
%%%%%%%%%%%%%%%%%%% State Equation Description %%%%%%%%%%%%%%%%%%
% Input: U = [Vg, Io];
% Output: Y = [Vo, Ig];
% State: X = [Ilr, Ilm, Vcr, Vcf];
```

```
%%%%%%%%%%%%%%%%%%%%%%%%%%%%%%%%%%%%%%%%%%%%%%%%%%%%%%%%
% define # of mode and dimension of output
num_mode = 4;
dim_out = 2;
% define harmonic table
% dc 1st 2nd 3rd
harm_tbl = [0 1 0 1; % Ilr-Ilm -- 1st state
0 1 0 1; % Ilm -- 2nd state
0 1 0 1; % Vcr -- 3nd state
1 0 0 0]; % vo - 4rd state
% define initial condition
x0 = [0; -2; -15; 11]; % [Ilr-Ilm; Ilm; Vcr; vcf]
% define Input variables
U0 = [40; 0]; % [Vg, Io]
% define control variables
Lr = 7.76e-6;
Cr = 470e-9;
Lm = 52.5e-6;
Cf = 20e-6;
rs = 0.01;
rc = 0.01;
Qs = 0.06; % Qs=Zo/R;
Fs = 80e3;
% Some parameters
Zo = sqrt(Lr/Cr); % Zo
Fo = 1/(2*pi*sqrt(Lr*Cr)); % Fo=83337 kHz;
R = Zo / Qs;
% Fsn = Fs / Fo;
k = R / (R+rc);
r = k * rc;
Ts = 1/Fs;
% define switching boundary conditions
if cur_mode == 1,
% set crossing boundary flag
if x(1) < 0.0 ,
switching = -1;
else
switching = 1;
end
% define piecewise linear state equations
A = [(-rs-r)/Lr, -rs/Lr, -1/Lr, -k/Lr;
```

```
r/Lm, 0, 0, k/Lm;
1/Cr, 1/Cr, 0, 0;
k/Cf, 0, 0, -k/R/Cf];
B = [1/Lr, -r/Lr;
0, r/Lm;
0, 0;
0, k/Cf];
C = [r, 0, 0, k;
1, 1, 0, 0];
D = [0, r;
0, 0];
% switching boundary condition:
% Ab * x + Bb * u + Cb * t + Db < 0
Ab = [1, 0, 0, 0];
Bb = [0, 0];
Cb = 0;
Db = 0;
elseif cur_mode == 2,
if t > 0.5 * Ts;
switching = -1;
else
switching = 1;
end
% define piecewise linear state equations
A = [0, 0, 0, 0;
0, -rs/(Lm+Lr) -1/(Lm+Lr), 0;
0, 1/Cr, 0, 0;
0, 0, 0, -k/R/Cf];
B = [0, 0;
1/(Lm+Lr) 0;
0, 0;
0, k/Cf];
C = [0, 0, 0, k;
0, 1, 0, 0];
D = [0, r;
0, 0];
Ab = [0, 0, 0, 0];
Bb = [0, 0];
Cb = 0;
Db = 0;
elseif cur_mode == 3,
```

```
if x(1) > 0,
switching = -1;
else
switching = 1;
end,
% define piecewise linear state equations
A = [(-rs-r)/Lr, -rs/Lr, -1/Lr, k/Lr;
r/Lm, 0, 0, -k/Lm;
1/Cr, 1/Cr, 0, 0;
-k/Cf, 0, 0, -k/R/Cf];
B = [-1/Lr, r/Lr;
0, -r/Lm;
0, 0;
0, k/Cf];
C = [-r, 0, 0, k;
-1, -1, 0, 0];
D = [0, r;
0, 0];
Ab = [-1, 0, 0, 0];
Bb = [0, 0];
Cb = 0;
Db = 0;
elseif cur_mode == 4,
if t > Ts,
switching = -1;
else
switching = 1;
end
% define piecewise linear state equations
A = [0, 0, 0, 0;
0, -rs/(Lm+Lr) -1/(Lm+Lr), 0;
00, 1/Cr, 0, 0;
0, 0, 0, -k/R/Cf];
B = [0, 0;
-1/(Lm+Lr), 0;
0, 0;
0, k/Cf];
C = [0, 0, 0, k;
0, -1, 0, 0];
D = [0, r;
0, 0];
```

```
Ab = [0, 0, 0, 0];
Bb = [0, 0];
Cb = 0;
Db = 0;
end
return;
end
```